공학박사학위논문

레이저 나노 구조 및 기계 지능에 기반한 인간-기계 상호 작용의 증강 전자 피부 개발

Augmented skin electronics for human-machine interaction based on laser nano structuring and machine intelligence

2021년 2월

서울대학교 대학원

기계항공공학부

김 권 규

레이저 나노 구조 및 기계 지능에 기반한 인간-기계 상호 작용의 증강 전자 피부 개발

Augmented skin electronics for human-machine interaction based on laser nano structuring and machine intelligence

지도교수 고 승 환

이 논문을 공학박사 학위논문으로 제출함

2020 년 10 월

서울대학교 대학원

기계항공공학부

김 권 규

김권규의 공학박사 학위논문을 인준함

2020 년 12 월

위 원 장 : 조규진 (인)

부위원장 : 고승환 (인)

위 원 : 이윤석 (인)

위 원 : 홍석준 (인)

위 원 : 이하범 (인)

Abstract

State monitoring of the complex system needs a large number of sensors. Especially, studies in soft electronics aim to attain complete measurement of the body, mapping various stimulations like temperature, electrophysiological signals, and mechanical strains. However, conventional approach requires many sensor networks that cover the entire curvilinear surfaces of the target area. We introduce two measuring system, novel electronic skins that could measure three dimensional touch information and dynamic human motions with a single sensor. Laser-induced multiscale structures of metal electrodes enable to achieve target sensitivity and performance. Moreover, deep-neural network successfully decodes the dynamic human motions. This technology is expected to provide a turning point in health-monitoring, motion tracking, and soft robotics.

Keyword : Skin-like sensor, laser nano structuring, machine intelligence

Student Number : 2016-34392

Table of Contents

List of Figures

Chapter I

Introduction

1.1 Background

The human-machine interface (HMI) provides a direct pathway between humans and machines. They have many roles in industries, healthcare, and entertainment (Figure 1). Recent advancements in soft sensors and actuators have unleashed the higher potential of HMI devices for its mechanical compliance, which provides a comfortable environment to the user.

An HMI is a bidirectional communication interface that is divided into human to machine (H2M) systems and machine to human (M2H) systems. H2M devices include sensors for measuring command signals such as touch, voice, and gesture, which allow for better system control, and measurement systems for measuring electrophysiological signals such as electromyography (EMG), electrocardiography (ECG), and electrooculography (EOG). M2H devices provide electrical, thermal, visual, or mechanical feedbacks that simulate various sensations. H2M control systems use sensors with various mechanisms. These include strain sensors that directly measure deformations owing to human motions or stretchable electrodes, which indirectly measure electric signals of the muscle. The performance of these sensors has been greatly improved in recent years through the integration of multiple functions, logic circuitry, and multi-dimensional detecting ability.

Although majority of soft HMI devices concentrate on H2M systems, M2H system with a stretchy form is on the rise owing to increased demand for wearable virtual and augmented reality (VR and AR) devices. These technologies include tactile feedback, thermal sensations, and wearable assistive devices. Since these system fabrications into stretchable forms require sophisticated technologies, only few reports of fully stretchable M2H devices exist. Recently, HMI device performances have been improved with the assistance of machine intelligence. These sophisticated electronic systems allow for the prediction of body motions with few sensors, detection of objects, and decoding neural command signals.

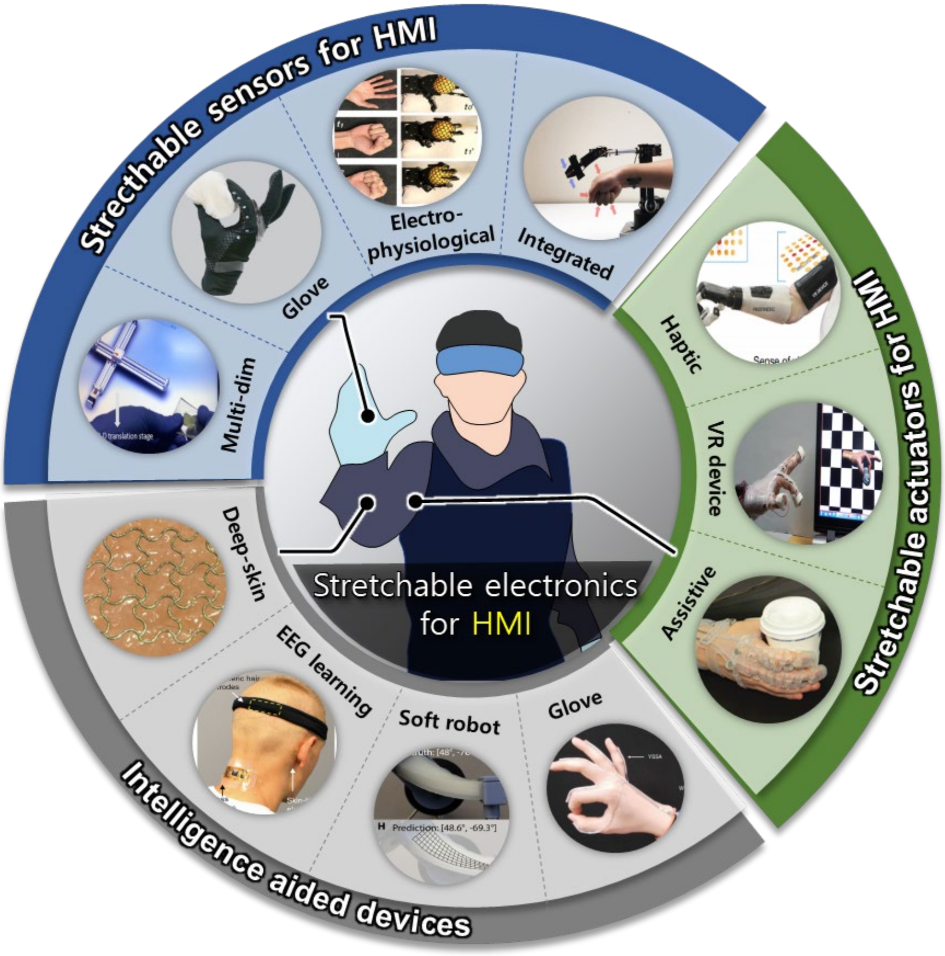

Figure 1. Compositions of flexible HMI devices.

As shown in Figure 2, length scale of the HMI devices decreases in order to achieve higher sensitivity. Nanoscale structures are required for measuring under few kPa pressure regions as depicted in Figure 3. Nanoscale enhances the sensing capability by concentrating electrons or pressure at the very edge of the pyramid[1-3] or dome-like structures[4-8], and nano cracks enables to achieve high mechano-sensitivity[9]. There are various patterning methods for HMI devices as shown in Figure 4; laser-based patterning method are superior to these methods since the process is done at low temperature and in a non-vacuum environment, which prevents significant damage of the flexible polymer from occurring during the process. However, the resolution of the laser-based patterning methods (visible laser sintering method) is limited to few microns, which are inadequate for nanoscale patterns for ultra-sensitive sensor applications.

Therefore, as shown in Figure 5, we included dynamic variations during the fabrication process. These include variations in fluid state of the nanomaterial (Marangoni flow), and external mechanical stress (displacement controlled bending) to the fabricated material.

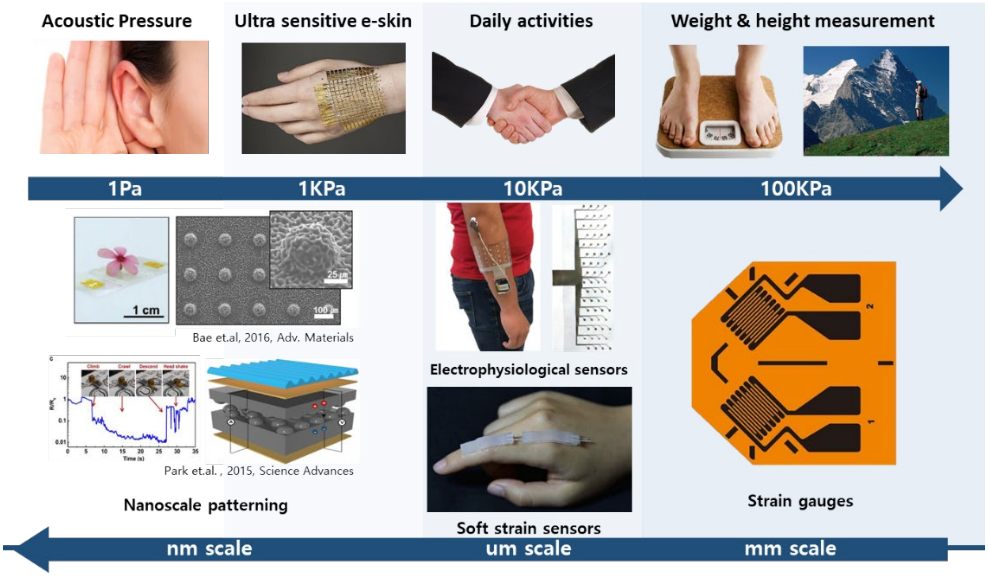

Figure 2. Scale of the electrode patterns according to the working region.

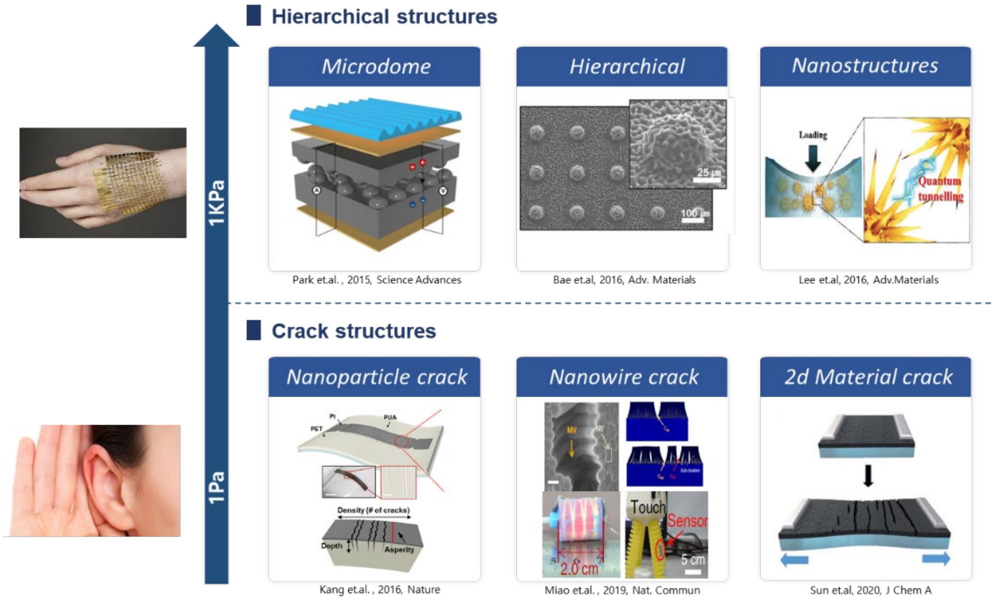

Figure 3. Nano scale patterns of the ultra-sensitive HMI devices.

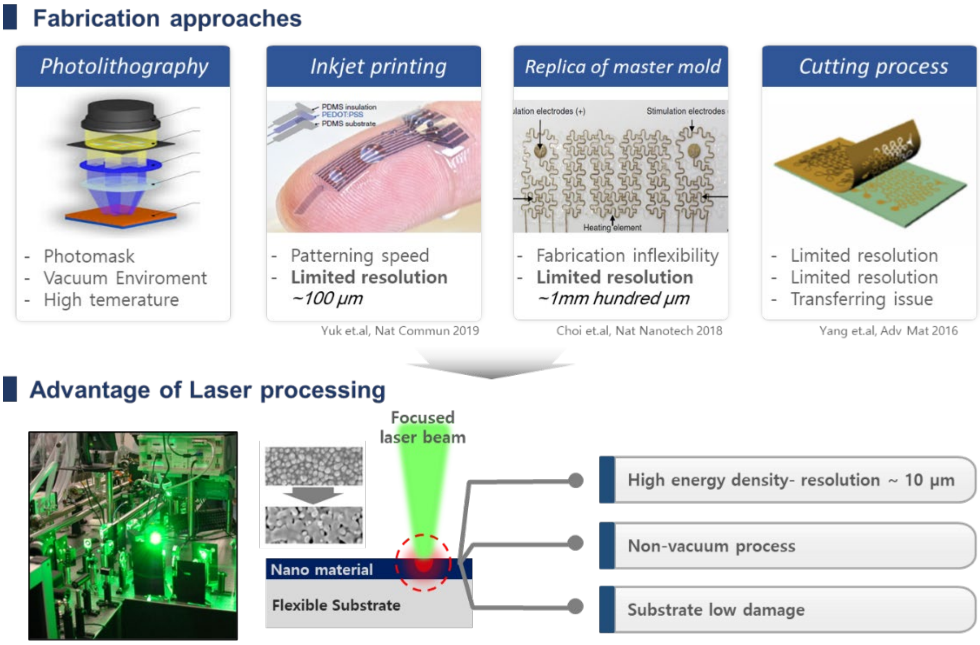

Figure 4. Advantage of laser processed electrode patterns.

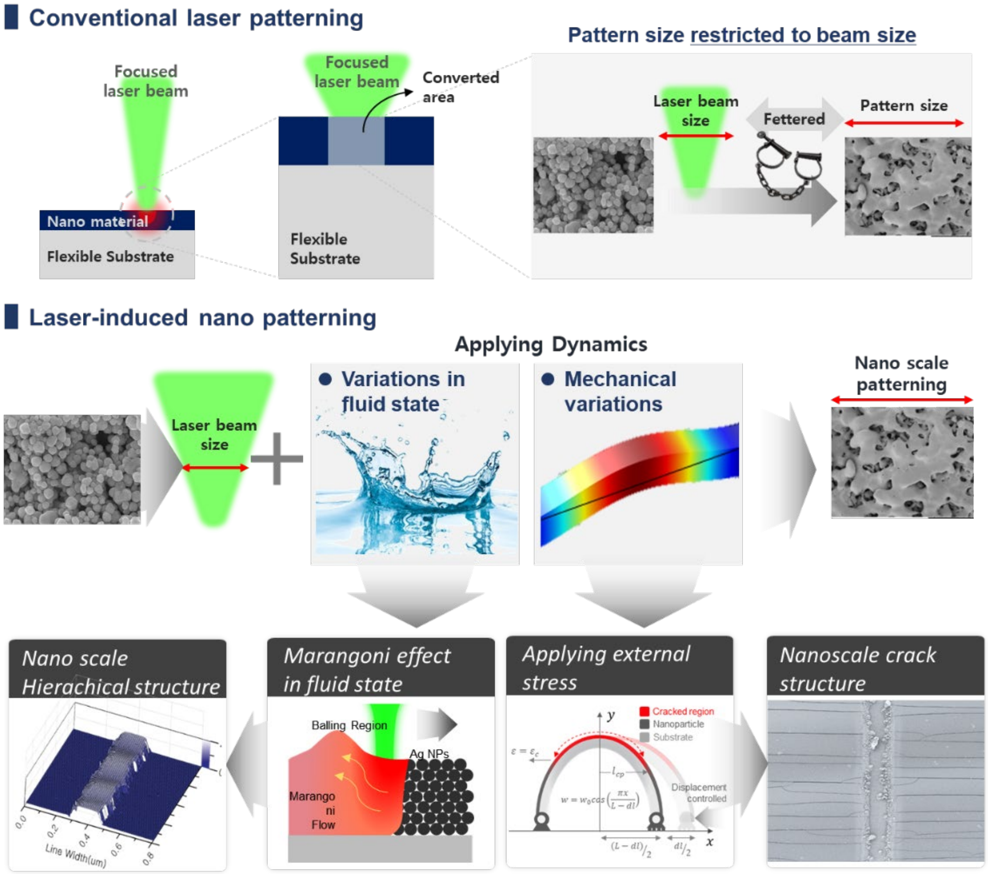

Figure 5. Comparison with the conventional laser patterning method.

1.2. Purpose of Research

The focus of this thesis is the development of skin-like human-machine interface (HMI) through laser-induced nano patterning. Sensors are augmented through nano-structuring of metal electrodes via dynamic laser thermal irradiation. New levels of sensor signal identification are also demonstrated with the aid of machine intelligence. The thesis includes the following area of research:

- Analysis of laser-induced multiscale Marangoni structure

- Analysis of laser-induced cracking of metal nanoparticles

- Wearable and transparent 3D touch applications

- Intelligence aided sensor decoding human motions

Chapter II

Laser-induced Marangoni structure

2.1 Fabrication of the multiscale structure

So far, non-flat surface morphology appearing in the selective laser sintering (SLS) process was considered to be a metallurgical defect, the so-called ‘balling effect’. However, controlling the irradiation parameter with the support of sophisticated physical analysis, the morphology can be easily manipulated to a desired structure. In this way, we developed a self-generated microstructure by laser-induced spatial thermal gradient. When the laser is scanned on the spin coated AgNP layer, a temperature difference arises between the laser spot center and the lag side. The temperature of the spot center is higher than the lag side, since the lag side has been cooled by the ambient environment. In this temperature distribution, the surface shear stress of the molten silver layer acts toward the relatively cold area, *i.e.,* the lag side, since generally the surface tension of common liquids decreases with increasing temperature. Consequently, surface force causes Marangoni convection flow, which circulates in the right-hand direction with respect to the out of plane direction (Figure 6c). This circulating flow plays a key role in determining the surface morphology of the resultant electrode during laser irradiation (Figure 6a). Since the surface morphology reconstruction caused by Marangoni flow occurs during the time when the AgNP layer remains in a liquid state, two time scales are major factors in laser-induced surface deformation: a time scale for Marangoni convection flow (τ_c) and the characteristic time in which the AgNP layer remains liquid (τ_{liq}). The temporal dependence of the surface temperature profile induced by laser irradiation is shown in Figure 6b**,** where τ_l, τ_m, and τ_s are the laser irradiated heating time, melting time, and solidification time, respectively. The gray area denotes the time interval in which the AgNP layer remains liquid ($\tau_{liq} = \tau_l + \tau_s - \tau_m$). The two time scales ($\tau_s$, τ_m) are negligible since they are relatively small compared to τ_l ; thus, the key time scales are

$$\tau_{\mathrm{liq}} \approx \tau_{\mathrm{l}} = \frac{L}{v_{\mathrm{scan}}} \qquad \textbf{(1)}$$

$$\tau_{\mathrm{c}} \sim \frac{L}{U} = \frac{\mu L^2}{|{}^{d\gamma}/_{dT}|\Delta T H}, \qquad \Delta T \sim \frac{\dot{Q}}{kH} \qquad \textbf{(2)}$$

where L is the characteristic dimension (laser spot radius, 10 μm), v_{scan} is the laser scan speed (200 mm s^{-1}), U is the characteristic Marangoni flow speed, μ is the viscosity of molten silver, $|d\gamma/dT|$ is the surface tension gradient with respect to the temperature of molten silver, H is the height of AgNP layer, $\dot{Q}$ is the laser power, and k is the thermal conductivity of the AgNP layer. We quantitatively investigated the surface deformation process by introducing the Surface shaping number (S) :

$$S = \frac{\tau_1}{\tau_c} = \frac{|{}^{d\gamma}/_{dT}|}{\mu L k} \frac{\dot{Q}}{v_{\mathrm{scan}}} \quad \textbf{(3)}$$

which is a dimensionless number defined as the ratio between τ_c and τ_l ($\approx \tau_{liq}$), indicating the speed of the circulating flow compared to the solidification rate. When a large spatial thermal gradient is established in the pristine AgNP surface, surface shear stress affects the interface between liquid silver and ambient air, making it energetically unstable. A small geometrical perturbation that inherently exists on the AgNP surface causes the molten silver surface to undergo a transition to an energetically favorable state, which tends to minimize the surface free energy. Such a transition rate is inversely proportional to the mass transportation characteristic time, τ_c. The process condition can be classified in to three cases depending on the value of S. Firstly, S < 1 (τ_c is larger than τ_l, Figure 6d). Since the molten silver cools down rapidly, solidification occurs before the unstable liquid silver interface initiates its transition. In this instance, surface reconstruction cannot occur, and the resultant electrode remains flat. Secondly, S ~ 1 (τ_c is comparable to τ_l, Figure 6e). Solidification and transition takes place simultaneously; thus, the silver is solidified and develop its structure during the intermediate morphological transition. Since the cycle of the reconstruction is analogous to the transition cycle, a regular wave structure is generated behind the laser scan direction. Lastly, S > 1 (τ_c is smaller than τ_l, Figure 6f). In this situation, enough time is provided to preserve the liquid phase. Since the initial geometrical perturbation is randomly distributed over the surface, this condition generates unbalanced spherical island structures, which is the lowest energy configuration of the interface. Since the laser profile and the shape are also important parameters determining the resultant surface morphology, further rigorous investigations should be required. The brief discussion regarding these parameters is found in Supplementary Note 6.

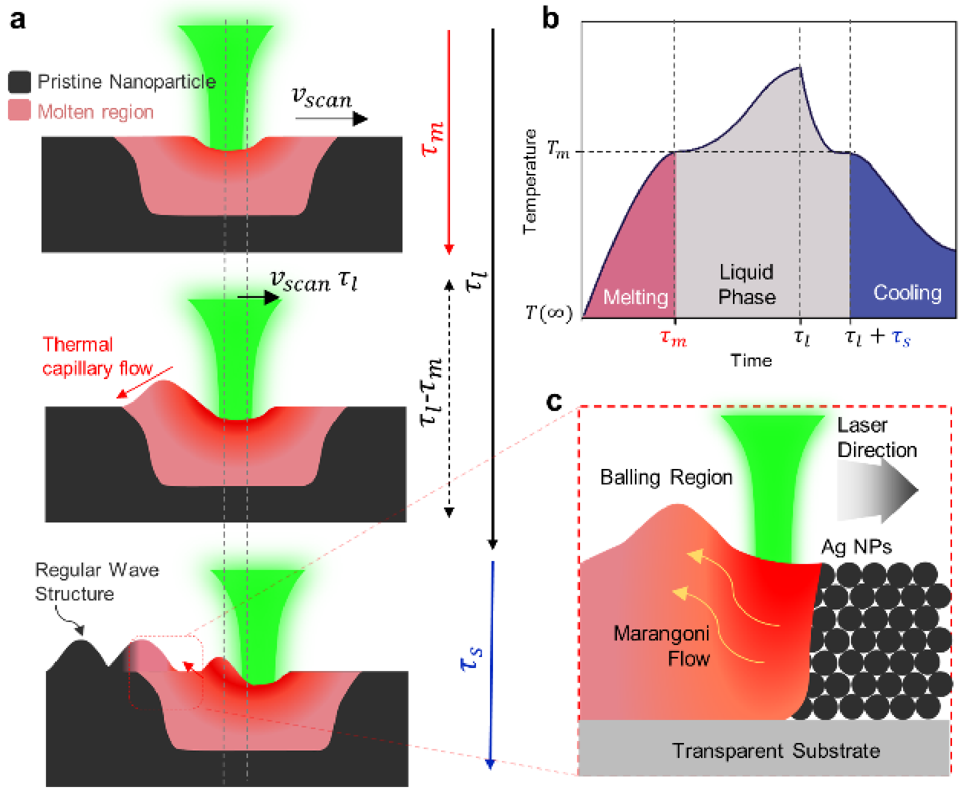

Figure 6. Self-generated multiscale structure by laser induced Marangoni flow. a, Time scales of micro thermofluidic phenomena under optimum conditions for regular wavy structure. b, Temporal dependence of characteristic temperature profile induced by single cycle of laser scanning. c, Marangoni convection in molten AgNP layer induced by laser scanning.

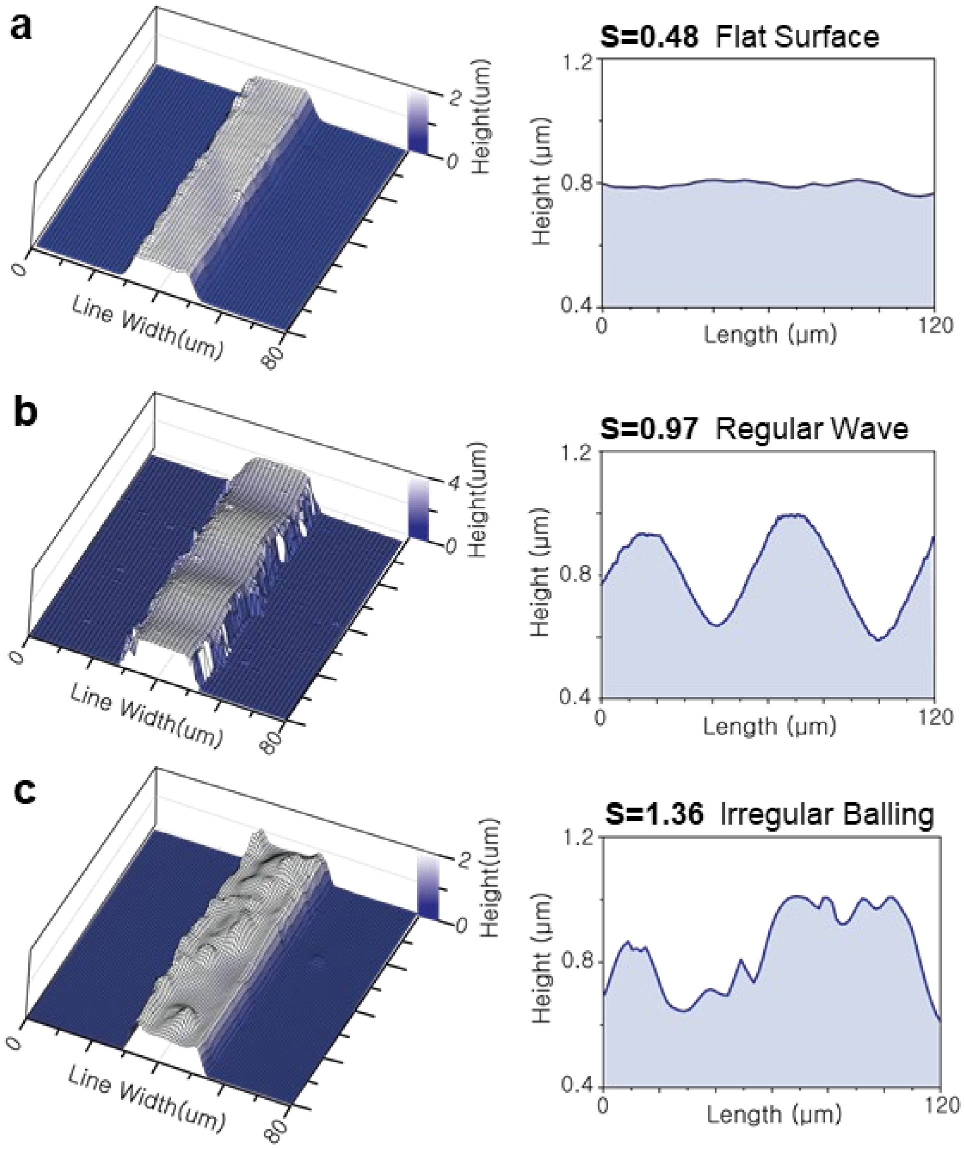

Figure 7. a-c, 3D scanned image and surface profile of AgNP layer with different laser conditions with S = 0.48 (a), S = 0.97 (b) and S = 1.36 (c).

2.2 Time scales regarding the temperature induced by laser irradiation

To irrustrate a thermal phenomenum during laser sintering, 'Lumped capacitance model' which can predict the temperature of solids experiencing a sudden change in its thermal environment[1] was employed. The model stands on the assumption which describes gradient of temperature field in a solid as zero, that is, thermal conduction in a solid would be negligible due to the fast changing of thermal environment. A situation of heat transfer for high conductive material can be also illustrated by such a way. Since the AgNP layer heated by laser irradiation also experiences extremely fast heat exchange, 'Lumped capacitance model' could explain the temporal change of representative temperature of the system. Basic derivation of the model starts from energy balance of control volume,

$$\rho c_{\mathrm{p}} V \frac{dT}{dt} = -hA(T - T_{\infty}) + \dot{Q} \tag{4}$$

where $\rho c_{\mathrm{p}} V$ is heat capacity of control volume, T is characteristic temperature, h is convective heat transfer coefficient, A is the area of heat exchange, T_{∞} is ambient temperature, and $\dot{Q}$ is volumetric heat input. With proper initial condition (say $T(0) = T_{\infty}$) for heating section (regime (i), (ii) in Figure 2b), above first order ordinary differential equation gives us the solution form of exponentials,

$$T(t) = \frac{\dot{Q}}{\rho c_{\mathrm{p}} V}\left[1 - \exp\left(-\frac{hA}{\rho c_{\mathrm{p}} V} t\right)\right] + T_{\infty} \qquad \textbf{(2)}$$

The solution for cooling part (regime (iii), (iv) in Figure 2b) can be obtained imposing an initial condition as $T(0) = T_{\mathrm{i}}$ with $\dot{Q} = 0$

$$T(t) = (T_{\mathrm{i}} - T_{\infty}) \exp\left(-\frac{hA}{\rho c_{\mathrm{p}} V} t\right) + T_{\infty} \qquad \textbf{(3)}$$

In consequence, the general temporal evolution of representative temperature of the system is expressed by exponentials having time constant related to heat capacity. In a one cycle of laser scanning, there are distinctive steps expected during evolution of temperature. Firstly, a solid AgNP layer is heated up until its melting point (regime (i)). The time required to melt a solid silver layer is defined as τ_{m}. Secondly, silver layer is heated until laser irradiation terminated (regime (i), (ii)). Laser time which heat input $\dot{Q}$ exists is indicated as τ_{l}. Note that each time constants of exponentials are different since heat capacity of solid silver is quite deviated from liquid silver's, and between two regions, constant temperature section must be inserted because of melting transition. After heating section (regime (i), (ii)), natural cooling (regime (iii), (iv)) would be occurred, time constants for each phase are same as heating section, but this statement is not inferring that rate of change of temperature is also same, since heating and cooling situation have different multiplied coefficient of exponential.

2.3 Marangoni convection flow characteristic time scale

When thermal gradient is induced by laser along scanning direction, circulating flow toward lag side would be driven by generated surface shear stress. We considered driving and drag forces acting on interface for determining the characteristic velocity of the flow in film layer. According to the lubrication theory, inertia terms in the Navier-Stokes equation could be negligibly small under condition that system we are interested has very small height compare to system characteristic length, *i.e.* film flow. In these circumstances, the force balance of differential surface can be read as follow.

$$\overleftrightarrow{\tau} \cdot d\mathrm{A} = \boldsymbol{\nabla}(\gamma) dA \quad \textbf{(4)}$$

where dA is infinitesimal area of heated region. Left hand side is viscous shear force where $\overleftrightarrow{\tau}$ is surface stress tensor and right hand side is driving force where $\boldsymbol{\nabla}(\gamma)$ gradient vector of surface tension. Since laser beam has radial symmetry, surface tension gradient acts effectively to x direction on z surface. Therefore, except τ_{xz} all other stress tensor component would be negligible. The force balance relation can be reduced considering only radial component (x direction),

$$\tau_{\mathrm{xz}} dA = \frac{d\gamma}{dx} dA \quad \textbf{(5)}$$

$$\mu \frac{du_{\mathrm{x}}}{dz} = \frac{d\gamma}{dx} = \frac{d\gamma}{dT}\frac{dT}{dx} \quad \textbf{(6)}$$

Applying the order-of-magnitude analysis to Supplementary equation 6,

$$\mu \frac{U}{H} \sim \left|\frac{d\gamma}{dT}\right| \frac{\Delta T}{L} \quad \textbf{(7)}$$

where μ is viscosity of liquid silver, U is characteristic velocity of Marangoni convection, γ is surface tension of liquid silver, and ΔT is characteristic temperature difference. Thus, the scaling of characteristic velocity of Marangoni convection becomes,

$$U \sim \frac{H\Delta T}{\mu L}\left|\frac{d\gamma}{dT}\right| \quad \textbf{(8)}$$

Finally, the scaling of characteristic time of Marangoni convection is that

$$\tau_{\mathrm{c}} \sim \frac{L}{U} = \frac{\mu L^2}{H\Delta T}\frac{1}{\left| {d\gamma}/{dT} \right|} \quad \textbf{(9)}$$

ΔT will be discussed in detail with heat transfer analysis, Supplementary Note 3.

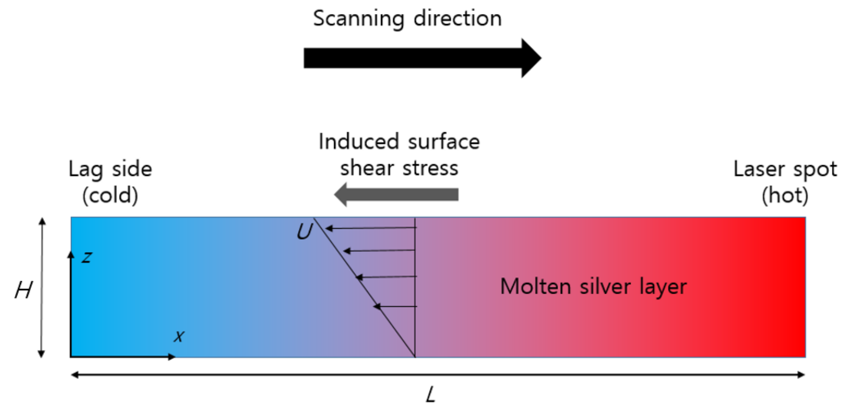

Figure 8. Schematic diagram of laser heated unit cell. The characteristic length of scanning direction, L is chosen to be half width of laser intensity, 10 μm. Layer height, H is 1 μm. The lubrication approximation can be applied; inner flow velocity profile is assumed linear.

2.4 Heat transfer consideration & thermal time scale

The order of temperature difference ΔT between the center of laser spot and lag side can be scaled by comparing magnitudes of each terms in integrated heat conduction equation.

$$\rho c_{\mathrm{p}} \frac{\partial T}{\partial t} = k\nabla^2 T + \dot{q} \tag{10}$$

where ρc_{p} is volumetric heat capacity of layer, k is thermal conductivity. Using geometrical and thermal remarks of molten silver layer system , integrated both side with respect to *x, z* direction,

$$\rho c_{\mathrm{p}} H \frac{\partial}{\partial t} \int_0^L T dx = kH \int_0^L \frac{\partial^2 T}{\partial x^2} dx + q'' L \tag{11}$$

$$\rho c_{\mathrm{p}} HL \frac{\partial}{\partial t} \Delta T = kH \left(\left.\frac{\partial T}{\partial x}\right|_{r=L} - \left.\frac{\partial T}{\partial x}\right|_{r=0} \right) + q'' L \tag{12}$$

The order of magnitude analysis transforms Supplementary equation 12 to

$$\rho c_{\mathrm{p}} HL \frac{\Delta T}{\tau_{\mathrm{l}}} \sim kH \frac{\Delta T}{L} + q'' L \tag{13}$$

$$\Delta \mathrm{T} \sim \frac{q'' L^2}{\frac{\rho c_{\mathrm{p}} HL^2}{\tau_{\mathrm{l}}} - kH} = \frac{q'' L^2}{(\rho c_{\mathrm{p}} v_{\mathrm{scan}} L - k) H} \tag{14}$$

$q'' = a q''_{\mathrm{laser}}$ where a is absorbance of silver at 532nm and q''_{laser} is irradiated laser heat flux. But temporal contribution term has one dimensional parameter that we treat as micro scale. For vivid picture of such a dimensional property of laser induced temperature field, we had investigated comparing laser scan speed and thermal conduction diffusion speed. With proper condition of laser micro process, we can expect thermal diffusion speed be much faster than scanning speed for concrete formation of electrode. Thus,

$$v_{\text{conduction}} \sim \frac{\alpha}{L} = \frac{k}{\rho c_{\text{p}} L} \tag{15}$$

$$\frac{v_{\text{scan}}}{v_{\text{conduction}}} \sim \frac{v_{\text{scan}} \rho c_{\text{p}} L}{k} \ll 1 \tag{16}$$

$$v_{\text{scan}} \rho c_{\text{p}} L \ll k \tag{17}$$

Under condition usually implemented in laser experiment, we could have checked above assumption, left hand side of inequality is $9.63\ \text{mW m}^{-1}\text{K}^{-1}$ while the right hand side is $180\ \text{W m}^{-1}\text{K}^{-1}$ which has 4 order of magnitude larger than left side (Supplementary Table 3). With this comparison, the characteristic temperature difference is expressed as:

$$\Delta T \sim \frac{q'' L^2}{kH} = \frac{\dot{q}}{kH} \tag{18}$$

Time scales related temporal change of temperature, $\tau_{\text{m}}, \tau_{\text{l}}$ and τ_{s} are compared for understanding major factor of the process. Each times are scaled by ratio between heat exchange rate and related heat amount except τ_{l} which can be scaled explicitly.

$$\tau_{\mathrm{m}} \sim \frac{\rho H L^2\{\varphi_{\mathrm{m}} + c_{\mathrm{p}}(T_{\mathrm{m}} - T_{\infty})\}}{\dot{q}} \qquad \textbf{(19)}$$

$$= \frac{\rho H\{\varphi_{\mathrm{m}} + c_{\mathrm{p}}(T_{\mathrm{m}} - T_{\infty})\}}{q''} \sim H$$

$$\tau_{\mathrm{l}} \sim \frac{L}{v_{\mathrm{scan}}} \sim L \qquad \textbf{(20)}$$

$$\tau_{\mathrm{s}} \sim \frac{\rho c_{\mathrm{p}} H L^2 \Delta T}{h L^2 \Delta T} = \frac{\rho c_{\mathrm{p}} H}{h} \sim H \qquad \textbf{(21)}$$

where φ_{m} is latent heat of silver for melting, T_{m} is the melting temperature of silver and h is convective heat transfer coefficient of AgNP layer. These relations show that τ_{l} is the largest time scale since $H < L \ll 1$ m, while other factors are intensive thermodynamic property except q''. Furthermore, other two time scale have large denominator compare to τ_{l}. Input laser heat flux q'' is extremely large from nature of laser irradiation, effective natural convective heat transfer coefficient, h is enhanced with large surface area. Meanwhile, calculation of time scales[2] verifies above observation.

$$\tau_{\mathrm{m}} = \frac{1}{\alpha}\left\{\frac{(T_{\mathrm{m}} - T_{\infty})k}{I_{\mathrm{a}}}\right\}^2 \text{, for surface absorption} \qquad \textbf{(22)}$$

Irradiated optical energy cannot propagate further the absorption length, the inverse of absorption coefficient for irradiated laser beam wavelength. When absorption length is very much shorter than thermal length of material, the optical energy converts to heat at the only thin layer whose height would be order of absorption length. The optical length of Ag for 532nm electromagnetic irradiation[3] is 12.3nm while thermal length is 13μm which has 3 order of magnitude larger than optical length.

Solidification time is expressed as,

$$\tau_{\mathrm{s}} = \frac{H^2}{4\zeta^2\alpha}\left(1 + \frac{2\zeta\sqrt{\alpha\tau_{\mathrm{l}}}}{H}\right) \quad \textbf{(23)}$$

Where ζ is the diemsionless constant, physically reasonable values within closed interval [0.25,1].

We calculated above three time scales[2] with following conditions: $v_{\mathrm{scan}} = 200\ \mathrm{mm\ s^{-1}}$ and $\dot{q} = 90\ \mathrm{mW}$. As expected, τ_{l} is dominant time scale in heating & solidification process (Supplementary Table 1), we concluded that the liquid time of AgNP layer is approximately equal to τ_{l}.

The surface morphology of AgNP layer is governed by the non-dimensional number S, ratio between Marangoni convection characteristic time τ_{c} and liquid time τ_{liq}. Following the logical step in Supplementary Note 1, 2, we determined the number S as below.

$$\mathrm{S} = \frac{\tau_{\mathrm{liq}}}{\tau_{\mathrm{c}}} = \frac{\left|{}^{d\gamma}/_{dT}\right|}{\mu L k}\frac{\dot{Q}}{v_{\mathrm{scan}}} \quad \textbf{(24)}$$

We fixed process speed, $v_{scan} = 200\ \mathrm{mm\ s^{-1}}$ ($\tau_{\mathrm{l}} = 50\ \mathrm{\mu s}$), the list of S for AgNP shown in Supplementary Table 2.

τ_m	τ_l	τ_s
0.117 ns	50 μs	2.76 μs

Supplementary Table 1. Calculated time constants

$\dot{Q}$(mW)	S (Surface shaping number)
10	0.097
50	0.48
100	0.97
120	1.16
140	1.36

Supplementary Table 2. Various S values in processing laser powers

Property (symbol)	Value	reference
Surface tension gradient ($^{d\gamma}/_{dT}$)	$0.1869\ \mathrm{mN\ m^{-1}\ K}$	[7]
Density (ρ)	$8600\ \mathrm{kg\ m^{-3}}$	[8]
Specific heat (c_p)	$0.28\ \mathrm{kJ\ kg^{-1}\ K^{-1}}$	[9]
Thermal conductivity (k)	$180\ \mathrm{W\ m^{-1}\ K^{-1}}$	[10]
Viscosity (μ)	$25.12\ \mathrm{mPa\cdot s}$	[11]
Absorbance (a)	0.47	Supplementary Figure 5

Supplementary Table 3. Thermofluidic properties of AgNP layer

2.5 Boundary condition between AgNP layer and substrate in heat transfer analysis

In derivation of characteristic temperature difference, ΔT, a heat flux across interface between AgNP and PET was treated as zero, i.e. adiabatic condition. This assumption can be verified by two unique natures of the process; 1) The processing time of laser melting is very short (50 μs) and 2) There is distinctive thermal diffusivity difference between AgNP layer and PET substrate. Within these conditions the heat provided by laser should not propagate through to the substrate. Comparing the propagated thermal lengths of each parts during 50 μs, the length for AgNP is about 26 times longer than the PET substrate (thermal length of the AgNP : 61.1 μm, thermal length of the PET substrate : 2.33 μm).

Furthermore, the time dependent FEM simulation (conditions are listed in Supplementary Table 5) was implemented for clear verification. As depicted in Supplementary Figure 3, simulated heat flow rate across the interface between AgNP and PET is negligibly small compared to the heat applied by laser irradiation, indicating that the majority heat exists in the high conductive region. Meanwhile, if the substrate has a high thermal conductivity, e.g. copper, thermal lengths of each materials should have the same order of magnitude, expecting that the heat flow propagates to both substrate and AgNP layer. We implemented the simulation replacing the substrate into Copper. The heat flow rate across interface was higher compared to the previous one, showing that 90 % of the irradiated power was propagated to the substrate (Supplementary Figure 3b).

Through above consideration, the boundary condition for the surface between AgNP layer and PET substrate can be approximated by adiabatic (i.e. insulated), and the heat transfer would be dominated by the AgNP layer.

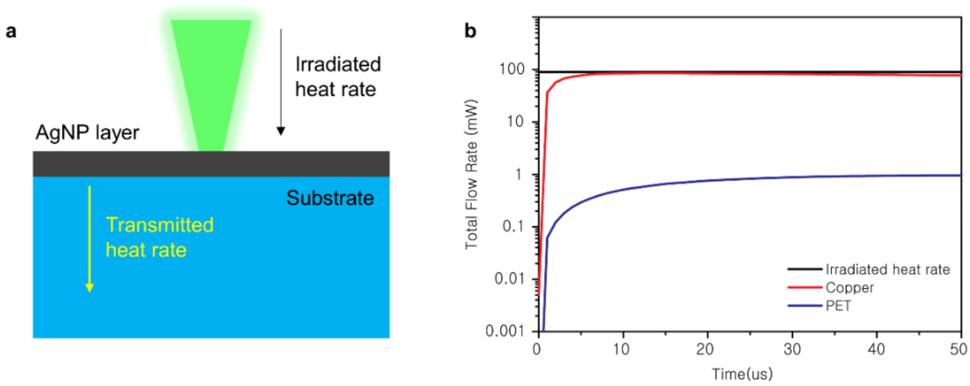

Figure 9. Simulation for verifying the adiabatic boundary condition. a. Irradiated heat rate is absorbed to AgNP layer, remained heat transmitted to substrate. b. The heat flows to the substrate in different ways depending on thermal diffusivity condition.

Chapter III

Wearable and Transparent 3D touch

3.1 Background of 3D touch

3D touch, also known as Force Touch, is a new field and becoming more widely valued in the market for its versatile function and outstanding interactions with users and accessibility to additional functionality by applying alternative touch motions. Commonly, spatial and pressure information are measured separately by simply combining two independent sensor components: a force sensor and a touch panel. Apple Inc. first released force touch technology in 2014[1], placing force sensors underneath the four corners of the rigid glass touch panel. In addition, researchers in academia developed various transparent pressure sensors[2-7] and integrated these sensors with commercial touch screen module[8]. However, the simply combined system has significant limitations; the sensing capability will be hindered if the force sensor is arranged at the bottom of the panel, and the transparency will be reduced in case that the force sensor is placed above the panel. Various tablet computers[9,10] are also capable of force sensing, which indeed functions only in the presence of its own extra stylus device. As stated above, a simple combination of different sensors is usually necessary to distinguish the position and pressure signals; hence, merging two functions in a single device is very challenging and causes various practical problems although a single device 3D touch that can simultaneously sense pressure and location will be the most ideal force touch device.

Besides, developing a force sensor operating under human touch motions is one of the key goals that address these challenges. Recently reported force sensors possess geometric features which contain conductive nanomaterials to obtain the required sensing ability[11-19]. The majority of them can be classified as pyramid[6,7,20] or dome-like structures[2,21-24], both of which concentrate the pressure or electrons at the very edge of the structure in order to enhance the sensing capability. Typical pressures produced by normal touch are distributed in the 10-100 kPa range[25,26], and since there is a strong relationship between the structure and the sensor performance, a concrete theoretical model that captures this relationship is necessary to describe the targeted pressure region, whereas previous studies have relied on simple analysis via curve-fitting[21,23].

3.2 Fabrication process of 3D touch

Figure 1 illustrates the entire fabrication process and structure of the 3D touch sensor. The sensor consists of two transparent layers and the fabrication of the upper layer is shown in Figure 10a. An ultra-thin silver nanowire (AgNW) network is uniformly sprayed onto the transfer material, covered with the desired mask pattern, and further embedded into UV curable polyurethane acrylate (PUA), the latter being designed to enhance the mechanical stability and surface flatness. Figure 10b shows a successfully fabricated free-standing transparent AgNW-PUA composite. Ultra-thin and long silver nanowires were synthesized by a polyol method with extremely high aspect ratio (30 nm thick and 50 μm long). The high aspect ratio nanowires significantly enhance the surface conductivity (~20 Ω/sq) while maintaining high transparency (>95%, Supplementary Figure 1) due to the decreased critical volume fraction of nanowires required to ensure a successive percolation network to achieve a conductive film[27-29]. The bottom layer consists of silver nanoparticles (AgNPs), which were also synthesized by a polyol method. The fabricated silver nanoparticle ink is first spin-coated on a PET substrate and then a 532 nm wavelength laser is focused at the AgNP layer to selectively convert the AgNPs into a continuous micro-sized comb-like metal pattern, as shown in Figure 1c. The aforementioned laser process is done at low temperature and in a non-vacuum environment which prevents significant damage of the flexible polymer from occurring during the process[30-32]. Since the sintered particles adhere strongly to the substrate, the surrounding residue could be easily removed by cleaning with polar solvents (e.g. water, ethanol). The transparent comb-like electrode fabricated by this process is depicted in Figure 11.

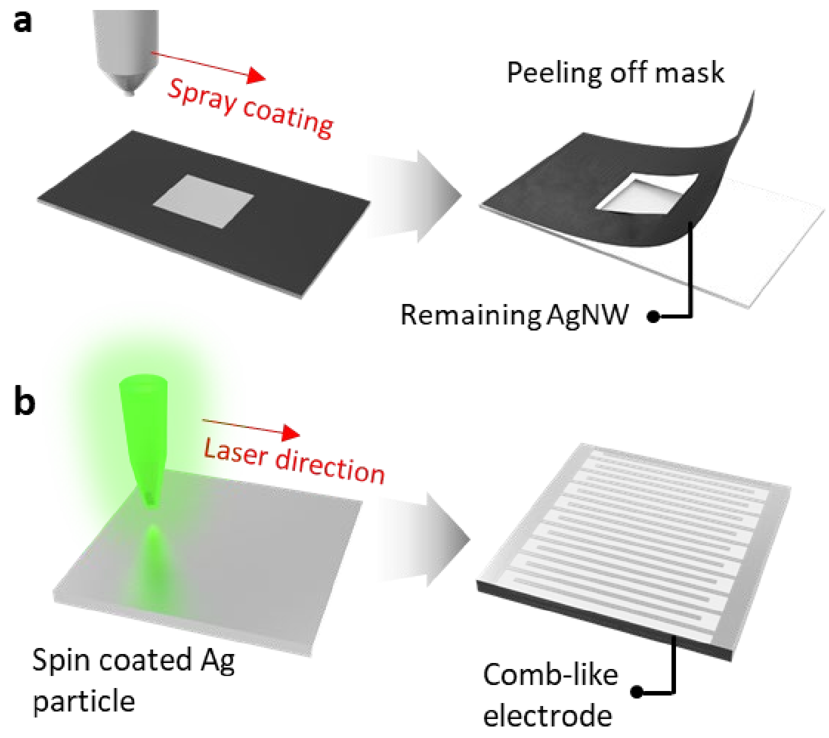

Figure 10. Fabrication of a wearable transparent 3D touch. a, Schematic depicting the fabrication of the upper transparent layer. b, Schematic depicting the fabrication of the lower transparent layer.

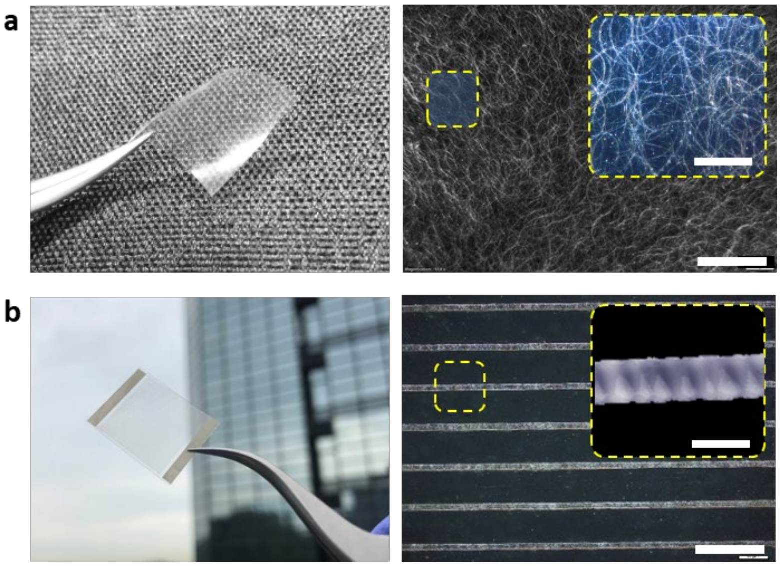

Figure 11. a, Free standing AgNW-PUA composite upper layer with SEM image. The inset in the right image shows a higher magnification image displaying the ultra-thin metal nanowire network. Scale bars, 150 μm and 50 μm (inset) b, Free standing AgNP comb-like lower layer with enlarged picture of an interdigitated electrodes. Inset shows a magnified image of the surface. Scale bars, 100 μm and 20 μm (inset)

The right image shows a microscope image of the patterned electrode with a 100 μm interval and 20 μm width. A higher magnification image is shown in the yellow-boxed inset. Both of the layers are then attached and encapsulated by PUA. The unique bi-layer sensor system is illustrated in Figure 12. Both the layers contribute to the excellent transparency (>85%); the transmittance (plotted on the left corner) was measured by UV-vis spectrophotometry. Macroscopically, the sensing mechanism is due to contact between the comb-like electrode array and silver nanowire percolation network. Microscopically, a higher external pressure forms a larger contact area between the percolation network and the self-generated corrugated structure along the electrode as demonstrated in magnified schematic, leading to more conducting pathways between the interdigitated electrodes. An overview of the sensor operation is provided in Figure 13. Arbitrary types of stylus such as a finger or any type of pen can be used to operate the sensor independent of the material's permittivity. The sensor system not only could measure the force but also recognize the contact position in simultaneous operation.

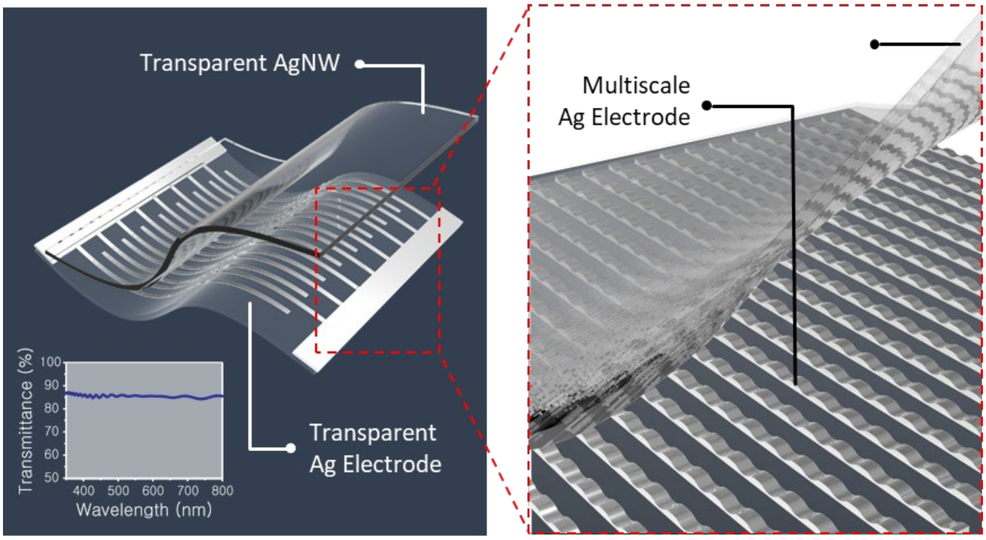

Figure 12. Schematic of the whole sensor system (Inset shows the transmittance of the system) with illustration of magnified image. Interdigitated lower electrodes are showing corrugated structure.

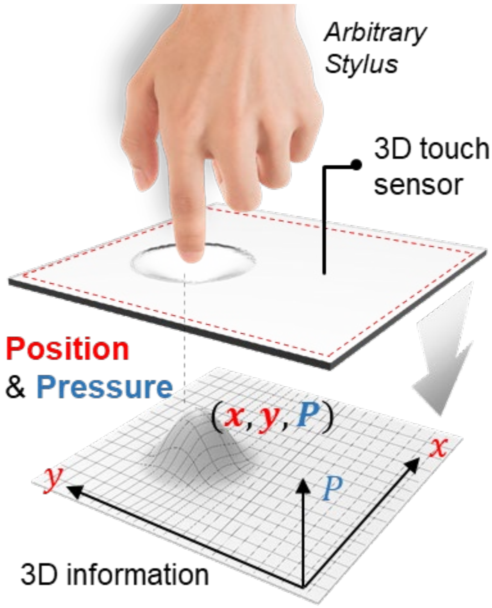

Figure 13. Illustration displaying the performance of the 3D touch.

3.3 3D touch applications

The working mechanism of the transparent 3D touch is illustrated in Figure 14. The sensor consists of six independent wires, four at the upper AgNW layer and two at the bottom interdigitated electrode. Wires are colored depending on their electrical status: potential input, voltage read, and open state. In order to detect the 3D signal, three steps of voltage switching are necessary. First, an equipotential distribution parallel to the x-axis is generated through the AgNW layer (X1-X2). The touched x-coordinate will be measured by the bottom read line (P1), detecting the voltage at the contact point. The bottom electrode is fabricated in the S ~ 1 condition, where the surface is regularly corrugated, which enables it to detect a wide range of pressures. In the same manner as the x-direction, the y-coordinate will be detected by applying a potential difference through the y-axis (Y1-Y2). After the coordinate detection, the electrode at the upper layer is switched as an open state, preventing current leakage through the upper electrode. Voltage is then applied in the remaining bottom electrode (P2), detecting the increased conducting pathways between the comb-like electrodes. As shown in Figure 15, the 3D touch was directly attached to the monitor screen and successfully able to draw a 3D structured object. We drew a continuous circle with increasing pressure, and a 3D structured spring was simultaneously generated on the screen. Furthermore, drawing a 3D structured G-clef was accomplished as depicted in Figure 16. An upper view of the G-clef is shown on the right corner, where the high-pressure region can be observed on the tail of the G-clef. As a proof-of-concept demonstration of its application as wireless wearable 3D touch, we combined the sensor with an integrated circuit board, MCU, and Bluetooth module as illustrated in Figure 17. The 3D touch was conformably attached to the forearm, and successfully transmitted the 3D information of a hand drawn star. To demonstrate the device's expandability, a sensor was fabricated with a sensing network of 100 pixels (10×10) consisting of 5 mm x 5 mm sized cells (Figure 18, V, R and S denote the voltage line, read line, and sensor, respectively). The sensor is capable of detecting a miniaturized PDMS foot, exhibiting an excellent pressure distribution. Also, four different pieces of PDMS forming the letters "ANTS" were placed on top of the sensor, showing a perfect pressure configuration, as shown in Figure 19.

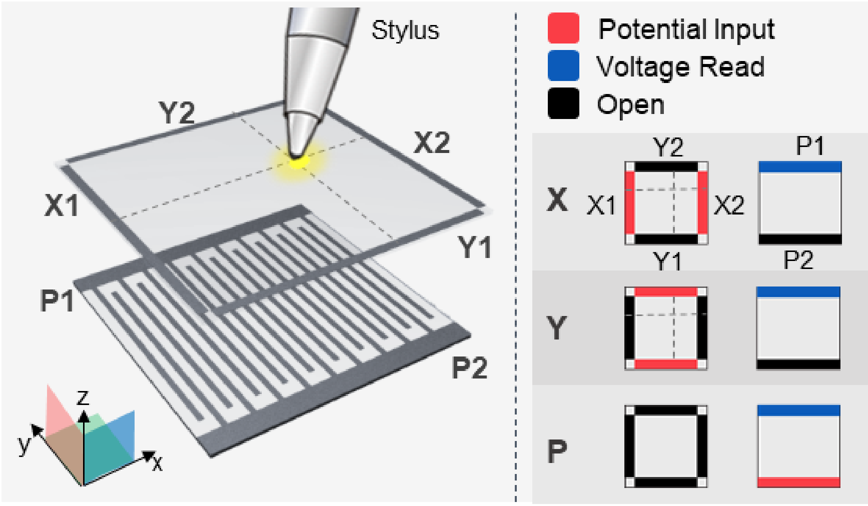

Figure 14. Working mechanism of 6-wire transparent 3D touch. b, 3D structured spring drawn by altering pen pressure

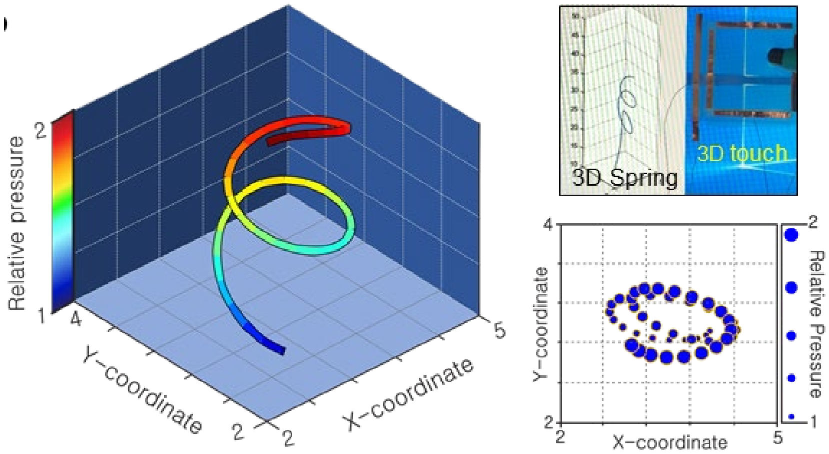

Figure 15. 3D touch was directly attached to a monitor while the spring is simultaneously displayed on the left. Also the pen pressure can be displayed as different line thicknesses as depicted on the right corner.

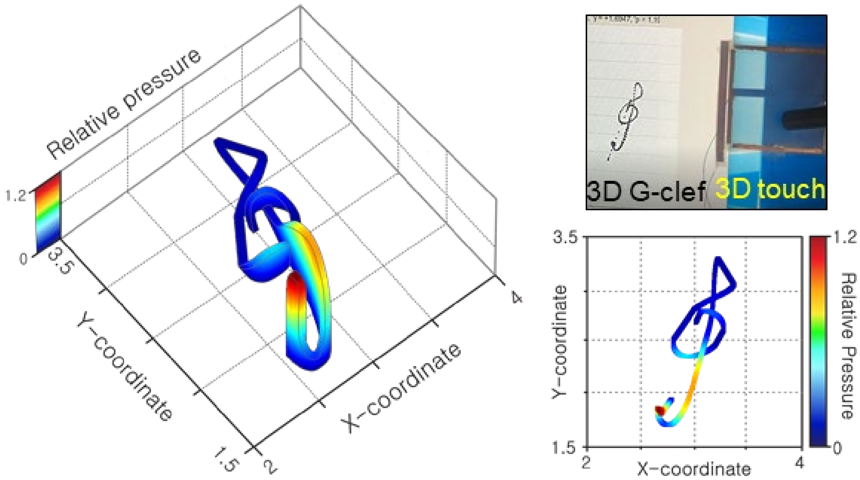

Figure 16. 3D structured G-clef drawn by 3D touch: 3D touch was directly attached to the monitor while the G-clef is simultaneously displayed on the left. The 2D figure of the G-clef is shown on the right corner.

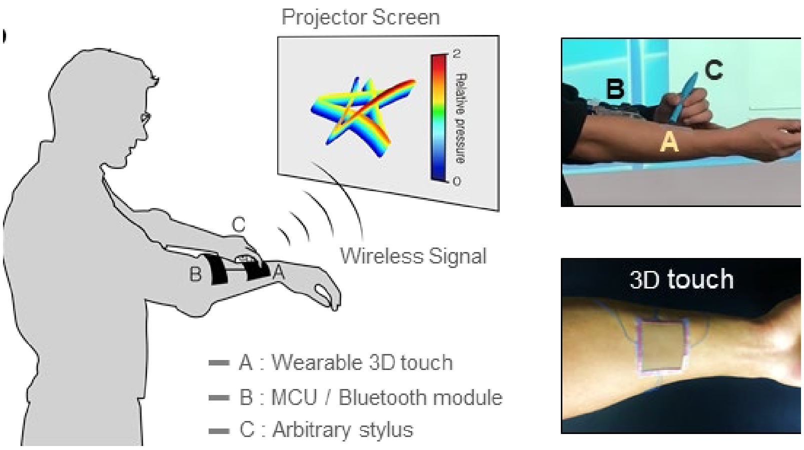

Figure 17. Demonstration as a wearable and wireless 3D touch: Illustration of drawing 3D structured star and the real image of the attached system on forearm.

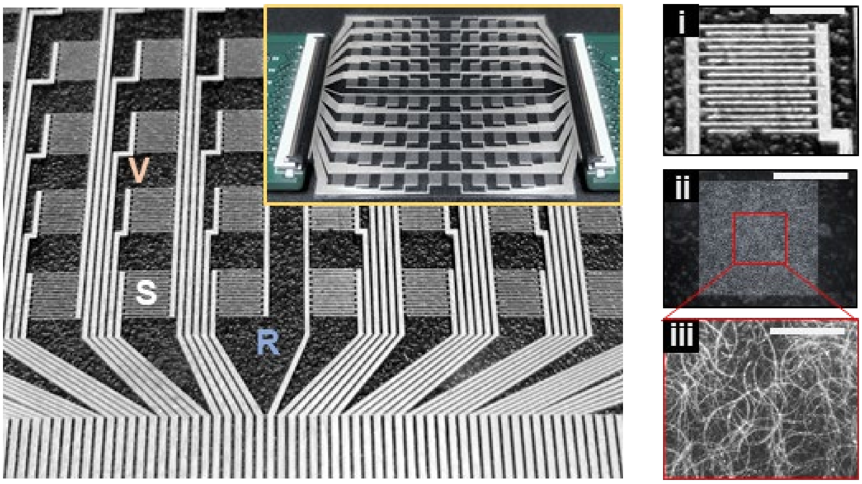

Figure 18. Picture of the 10×10 sensory array and the inset shows the entire system connected to the analyzer. Magnified image of a single cell containing comb-like electrode. Scale bar, 3 mm.

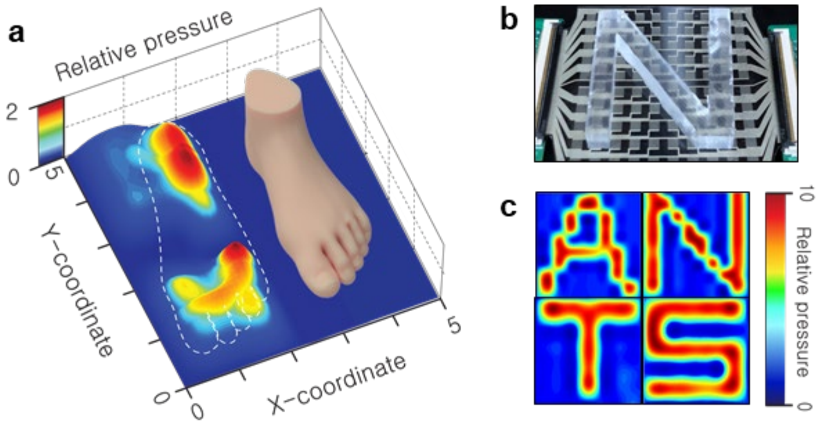

Figure 19. a, 3D pressure distribution of an artificial foot. Exact scale of the foot is compared next to the distribution. b, Sample image of PDMS block forming the letter ‘N’ placed on top of the sensor array. c, Pressure configuration showing the letters ‘A’, ‘N’, ‘T’, and ‘S’.

Chapter IV

Theoretical Analysis of the Multiscale Structure

4.1 Background of 3D touch

The output signal of the sensor is mainly dictated by two factors, the pressure-dependent contact surface between the layers and the consequent change in the electrical path. A theoretical model based on contact mechanics and geometrical resistance analysis was constructed in order to predict these processes. A magnified illustration of the comb-like electrode in the red box (Figure 20a). The geometric modeling parameters of the sensor are illustrated in the magnified images of three different views (Figure 20b). As shown in the XZ plane view, the repeating unit of corrugated structure could be estimated as a single sinusoidal wave, where δ is the amplitude of the wave, λ is the wavelength, and a is the projected length of the contact area. Since the modulus of the lower layer (comb-like electrode on the polymer substrate, E_{lower} = 83 GPa) is much higher than that of the upper layer (AgNW-PUA composite, E_{upper} = 20 MPa), the lower layer can be considered as a rigid body; hence, we could consider that there would be a linear elastic deformation of the AgNW composite above the rigid corrugated surface. Since the nanowire is randomly distributed over the polymer and could be treated as a continuous metal layer, the nanowire concentration would not significantly affect the output signal of the sensor. Therefore, the change in contact area directly affects the bridging current between the interdigitated electrode, shown in the YZ plane view, where w is the width of the electrode and d is the distance between the neighboring electrodes. The bridging current between the electrodes is shown in the XY plane view, and the current density is calculated by numerical simulation. Relations between the two-dimensional average pressure (P) and normal displacement ($u_z(x) = \delta\cos(2\pi x/\lambda)$) can be derived by solving the two-dimensional problems of an elastic half-space,

$$P[\mathrm{N\ m^{-1}}] = \frac{\pi^2 E\delta}{\lambda(1-\nu^2)}\left[\frac{1}{1!}\left(\frac{2\pi}{\lambda}\right)a^2 J_1 - \frac{1}{3!}\left(\frac{2\pi}{\lambda}\right)^3 a^4 J_3 + \frac{1}{5!}\left(\frac{2\pi}{\lambda}\right)^5 a^6 J_5 - \cdots\right] \quad \textbf{(4)}$$

The series J_n and the functional form of the actual contact area a_t are also given. As demonstrated in Figure 21, the relation between the contact length and conductance should be considered to further develop the relationship between the external pressure and output current signal of the sensor. As shown in Figure 22, a higher pressure generates more conducting pathways, which causes an increase in the output current at a fixed supply voltage. However, since the equipotential line is non-linear, the conductance cannot be easily calculated by the simple electric conductance relation, $G = \sigma A/l$, where σ is the conductivity, A is the cross-sectional area, and l is the length of the conductor. In this situation, the conductivity could be calculated by mapping every point of the physical plane (Z-plane) conformally to a corresponding auxiliary plane (χ-plane), the so-called, conformal representation. Among such methods, we used the Schwarz-Cristoffel transformation. By transforming the extremities of the contact area on the Z-plane, the equipotential line becomes linear on the χ-plane. Consequently, the geometrical resistance (G) can be approximated as

$$G \cong \frac{K'(k)}{K(k)}, \qquad k \cong \tanh[(\frac{\pi}{2}\left(\frac{Y}{X}\right)] \qquad \textbf{(5)}$$

where $X = l/l'$, $Y = a_t/l'$, and K denotes a complete elliptic integral of the first kind. A detailed derivation and an approximation of single cell conductance can be found. Since the entire sensor system is a combination of these micro cells, the total conductance of the sensor can be calculated by a parallel sum approximation. Therefore, the total conductance is given by

$$C_{\mathrm{t}} = N\sigma t \frac{1}{G} \sim \mathrm{O}(10^{-1}) \frac{1}{G} \quad \textbf{(6)}$$

where N is the number of corrugated micro cells O(10^2), σ is the conductivity of AgNW network O(10^4) S/m and t is the thickness of the AgNW layer O(10^{-7}) m. Thus, the correction factor is on the order of 10^{-1} in SI units. Taking the correction value of 5.6^{-1} and combining Equations 4 and 6, we could finally deduce the theoretical model of the sensor which explains the relation between the pressure and output current signal. Theoretical values were found to match perfectly with the experimental values, as depicted in Figure 23. To further investigate the performance of the sensor, we controlled two parameters, δ and d, which are amplitude and distance, respectively. An electrode with a flat surface ($\delta = 0$) operates as a contact between metal plates, i.e., the contact will form instantly. The pressure sensitivity seems to be extremely high; however, the sensing range is relatively small (<10 kPa). As a demonstration, a flat surface sensor is capable of detecting consecutive loading of five micro capacitor chips (5 μg each), where the inset shows the sensor and the micro capacitor chip compared with a US quarter coin (Figure 24). An electrode with a corrugated surface ($\delta = 100$ μm), has an enhanced sensing range, attributed to the multiscale structure, which makes it possible to detect inputs in the high-pressure regime (10-100 kPa) produced by daily life[25,26], and the applications of this structure will be covered. The distance between the electrodes also affects the sensor performance, as shown in Figure 25. A narrower electrode approaches the metal plate, and due to the same phenomenon above, increased sensor sensitivity can be observed in the figure. Furthermore, the sensor endures 30,000 pressure cycles with 24 ms response time (Supplementary Note 13). These results successfully demonstrate the accurate performance of the sensor, and from the theoretical analysis, the performance of the sensor is freely adjustable and can be implemented in various applications for different purpose.

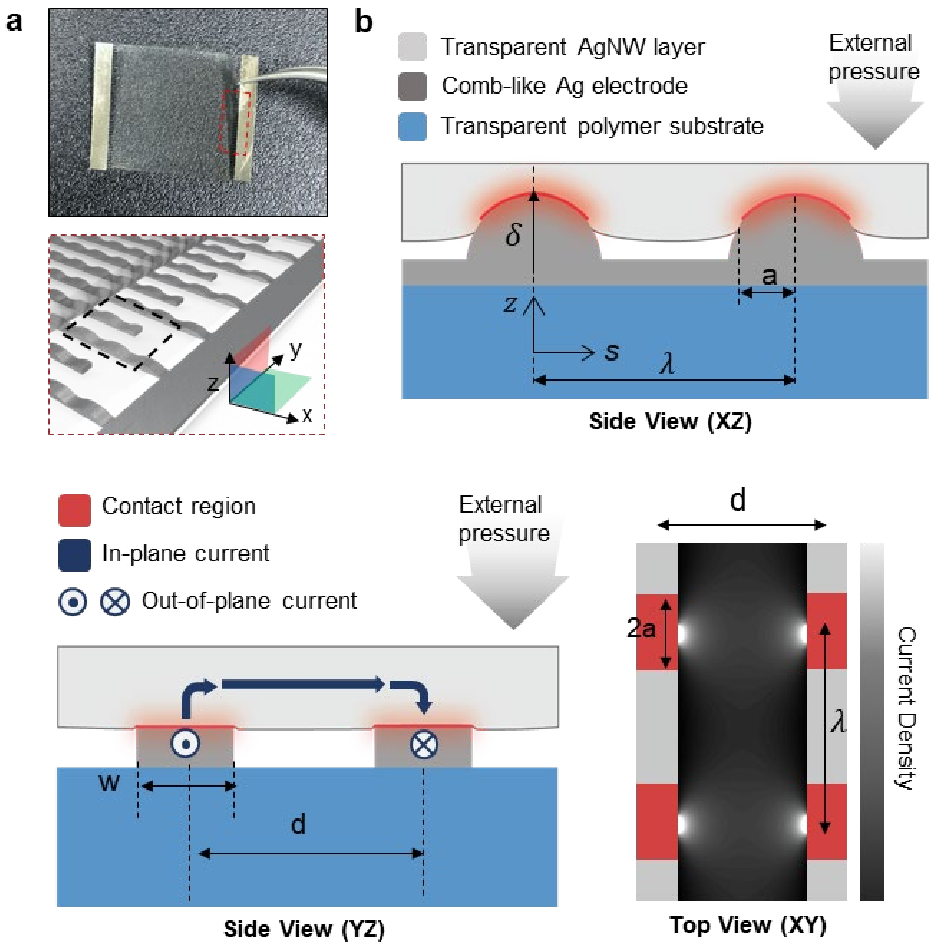

Figure 20. Theoretical analysis of the sensor. a, Picture of free-standing lower comb-like electrode with magnified image in which the black dashed box denotes the control surface. b, Illustration of electro-mechanical phenomenon with respect to the three different views in the control surface. XZ plane side view (left), YZ plane side view (center), and XY plane top view (right). XY top view containing simulation image of current distribution over the AgNW layer.

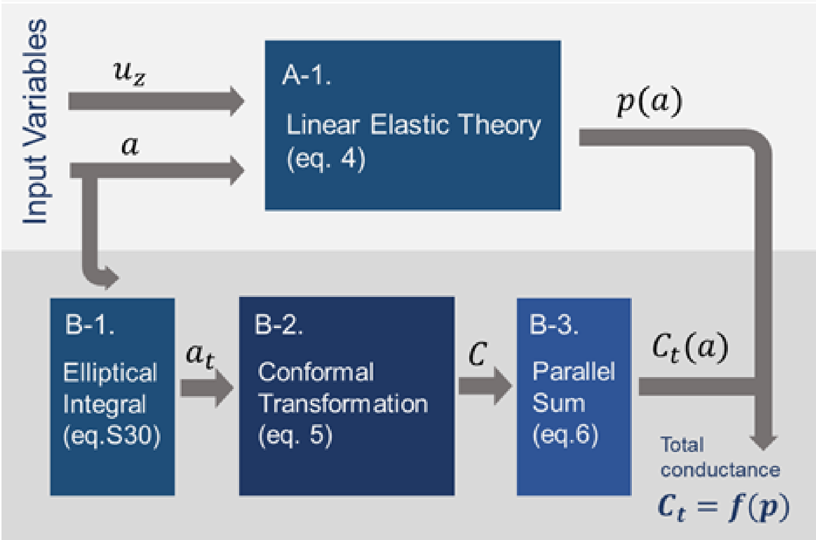

Figure 21. Diagram of the theoretical analysis.

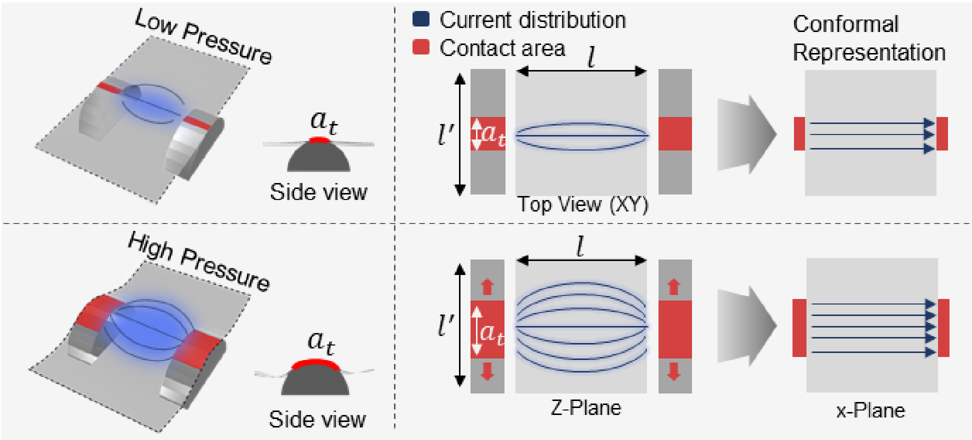

Figure 22. Schematics of the adjusted current distribution according to different external pressure and contact area. Right side denotes the conformal representation of the equipotential line.

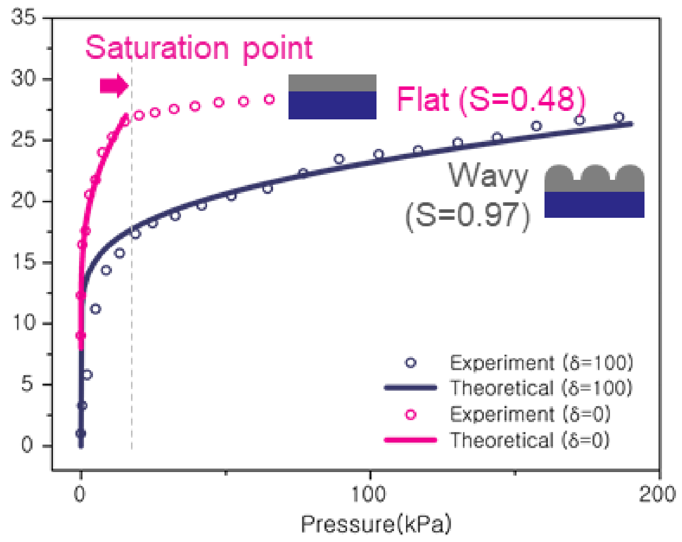

Figure 23. Current change for different surface morphology and comparison between the theoretical data from equations 4 and 6.

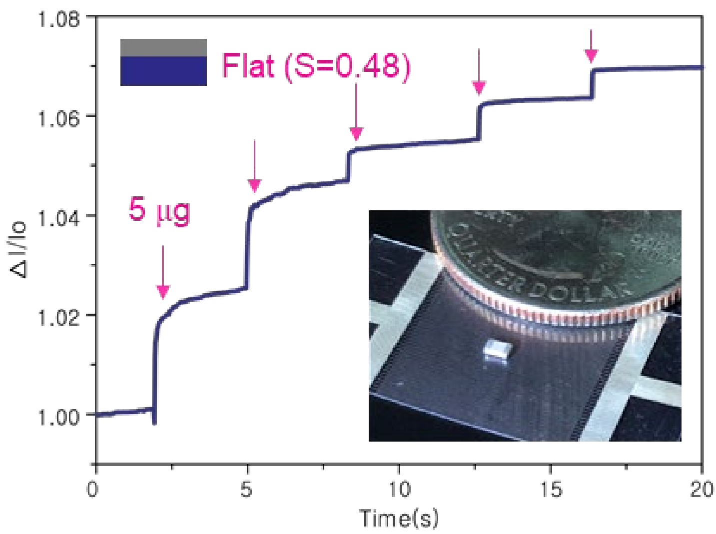

Figure 24. Demonstration as a high sensitive sensor (flat morphology, S = 0.48).

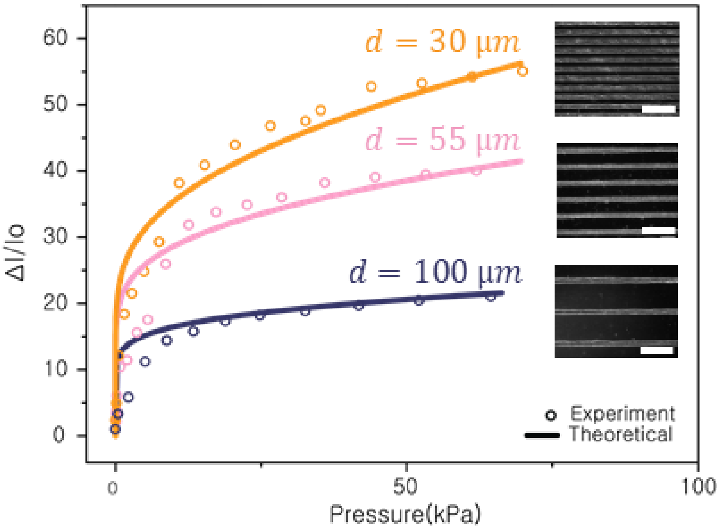

Figure 25. Output signal distribution as a function of electrode distance compared with the theoretical data.

4.2 The relation between contacted area and applied pressure

The contact problem of elastic body with rigid arbitral surface was investigated for model the situation of operating the sensor. In condition that $\frac{\delta}{\lambda} \ll 1$, shear strain of upper layer is negligible so that longitudinal strain should be dealt dominantly. Relations between the two-dimensional average pressure, $p(x)$ and normal displacement, $u_{\mathrm{z}}(x)$ can be derived as followed[4]:

$$\int_{-a}^{a} \frac{p(s)}{x-s} ds = -\frac{\pi E}{2(1-\nu^2)} \frac{du_{\mathrm{z}}}{dx} \tag{26}$$

If we let the right hand side be $\mathrm{g}(x)$, made up from a combination of material parameters and displacement gradient, the equation has a general solution of the form[5] as

$$p(x) = \frac{1}{\pi^2\sqrt{a^2-x^2}} \int_{-a}^{a} \frac{\sqrt{a^2-s^2}g(s)}{x-s} ds + \frac{C}{\pi^2\sqrt{a^2-x^2}} \tag{27}$$

where C is integral constant which denotes the average pressure among the contact region ($\mathrm{C} = \pi \int_{-a}^{a} F(s)ds$). If we take The equation above can be solved in which that u_{z} is of polynomial form : $u_{\mathrm{z}}' = -A_{\mathrm{n}}\mathrm{x}^{\mathrm{n}}$. Sinusoidal displacement, $u_{\mathrm{z}} = \delta\cos(\frac{2\pi}{\lambda}x)$, can be expressed as polynomial form by Taylor series. The pressure distribution for single term of polynomial nth power ($u_{\mathrm{z}}' = -A_{\mathrm{n}}x^n$) is shown as

$$p_{\mathrm{n}}(\mathrm{x}) = -\frac{EA_{\mathrm{n}}a^{n+1}}{2(1-\nu^2)\pi}\frac{I_{\mathrm{n}}}{\sqrt{a^2-x^2}} + \frac{P_{\mathrm{n}}}{\pi\sqrt{a^2-x^2}} \quad \textbf{(28)}$$

$$I_{\mathrm{n}} = \pi\left\{\left(\frac{x}{a}\right)^{n+1} - \frac{1}{2}\left(\frac{x}{a}\right)^{n-1} - \frac{1}{8}\left(\frac{x}{a}\right)^{n-3} - \cdots - \frac{1\cdot 3\cdot 5\cdots(n-3)}{2\cdot 4\cdots n}\frac{x}{a}\right\}$$

for even n,

$$= \pi\left\{\left(\frac{x}{a}\right)^{n+1} - \frac{1}{2}\left(\frac{x}{a}\right)^{n-1} - \frac{1}{8}\left(\frac{x}{a}\right)^{n-3} - \cdots - \frac{1\cdot 3\cdot 5\cdots(n-2)}{2\cdot 4\cdots(n+1)}\right\} \quad \textbf{(29)}$$

for odd n,

Using the continuity boundary conditions ($p(a) = p(-a) = 0$) and conditions for avoiding the singularity of the equation, the relation between the average external pressure (P_{n}) for single term of polynomial and projected contact length (a) can be derived as

$$P_{\mathrm{n}} = \frac{Ea^{n+1}}{2(1-\nu^2)}A_{\mathrm{n}}I_{\mathrm{n}}(a) \quad \textbf{(30)}$$

we set the coefiicient A_{n} be counterpart of expanded cosine function,

$$A_{2\mathrm{n}-1} = \frac{2\pi\delta}{\lambda}\left(\frac{2\pi}{\lambda}\right)^{2n-1}\frac{(-1)^{n-1}}{(2n-1)!} \quad \textbf{(31)}$$

$$A_{2\mathrm{n}} = 0$$

The final expression of nth approximated external pressurue should contain from 1 to n terms.

$$P = \sum_{n=1}^{\infty} P_{\mathrm{n}} \\ = \sum_{n=1}^{\infty} \left[\frac{E a^{2n}}{(1-\nu^2)} \frac{\pi\delta}{\lambda} \left(\frac{2\pi}{\lambda}\right)^{2n-1} \frac{(-1)^{n-1}}{(2n-1)!} I_{2\mathrm{n}-1}(a) \right] \tag{32}$$

This relation can be expressed identical to equation 1 in manuscript.

$$P[\mathrm{N\ m^{-1}}] = \frac{\pi^2 E\delta}{\lambda(1-\nu^2)} \left[\frac{1}{1!}\left(\frac{2\pi}{\lambda}\right) a^2 J_1 - \frac{1}{3!}\left(\frac{2\pi}{\lambda}\right)^3 a^4 J_3 + \frac{1}{5!}\left(\frac{2\pi}{\lambda}\right)^5 a^6 J_5 - \cdots \right] \tag{33}$$

where $J_{\mathrm{n}} = 1 - \frac{1}{2} - - \frac{1}{8} - \cdots - \frac{1\cdot 3\cdot 5\cdots(n-2)}{2\cdot 4\cdots(n+1)}$

To construct the relation between external pressure and conductance, one should consider converting the projected area (a) to actual contact length (a_t). The relation between actual contact length (a_t) and projected length of contact area (a) can be given by

$$a_t = \frac{\lambda}{\pi} E\left(\frac{2\pi}{\lambda} a \middle| - \left(\frac{2\pi\delta}{\lambda}\right)^2\right) \tag{34}$$

where $\mathrm{E}(\mathrm{x}|\mathrm{k}^2)$ is the elliptic integral of the second kind with parameter k^2. Actual contact length directly affects the bridging current between the electrodes.

4.3 Parallel micro resistance approximation

The micro resistors appeared by the external pressure are arranged along interdigitated electrodes periodically (Figure 26a). When the interval between cells is larger than contact area, $a_{\mathrm{t}} \ll \lambda,$ electrical current started at one side of micro resistance flows heading to its facing counterpart (Figure 26b). So that some cell of micro resistor cannot influence electrically to another cell. Therefore, the total impedance of one pair of interdigitated electrode can be approximated as an impedance of parallel connection of single cells. The charge conservation equation was solved by a simple FEM to confirm the independence between each cells (Figure 26c, d). The horizontal current density was visualized to show distinct electrical separation of each cells. In a typical sensor working range, the error between total resistance and parallel approximation was only about 4.34%.

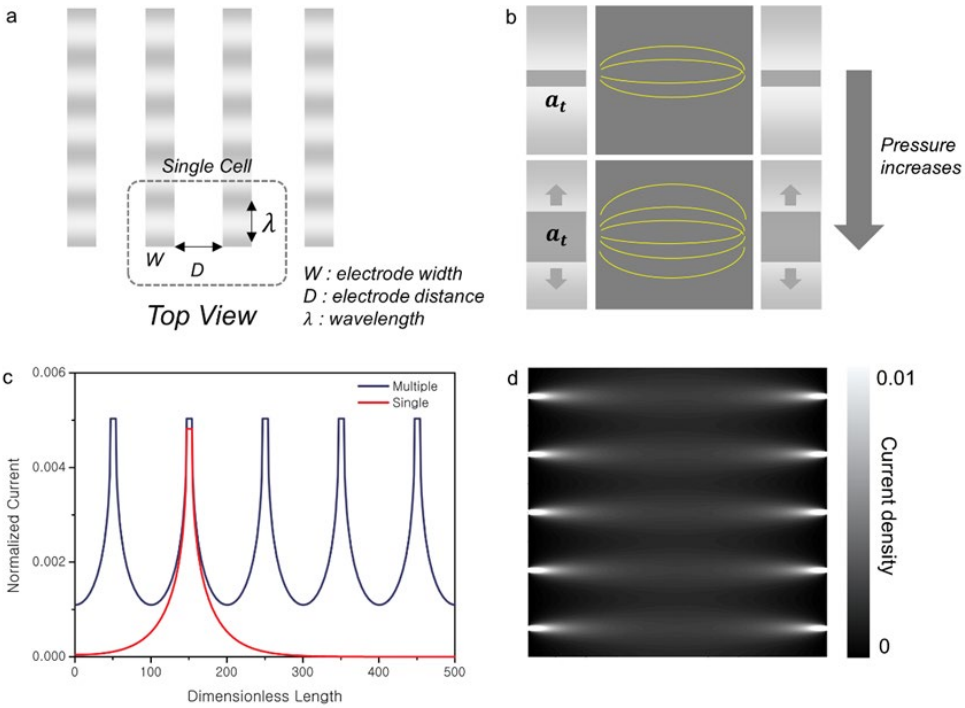

Figure 26. Simulation of the parallel micro resistance. a. Repeated unit cell of interdigitated electrode. Periodical distance is its wavelength λ. b. Nonlinear stream line of electrical current of each single cell. As applied pressure increases, contact area a_t is also magnified resulting larger conductance. c. Vertical current density averaged along horizontal direction. The current density of single micro resistor enveloped by current density of multiple network. Normalized resistance of single cell is 2.38 while multiple's is 0.498. d. 2D view (same as supplementary Figure 2b) of current density of multiple network. Each cell's current distribution is well isolated.

4.4 Calculation of single cell micro resistance

Unlike the usual rectangular resistor where the equipotential line is parallel to the electrodes, the micro resistors between interdigitated electrodes have nonlinear equipotential contour. The geometrical resistance can be obtained analytically using the Schwarz-Cristoffel mapping to calculate the resistance of such resistors[12]. Specify the position of vertexes defining geometry in the complex plane. The vertexes of micro resistor cell as P, Q, R, and S. resistor's electrode position is identified by A, B, C, and D. Through three conformal mapping steps (Figure 27), it is possible to convert the physical plane, Z-plane to imaginary one, χ-plane whose equipotential line is parallel to each other. With property of conformal transformation, conservation of local angle preserves the geometrical resistance. First step of transformation is that Z-plane to t-plane by following manner.

$$\mathrm{t} = \mathrm{sn}^2(mz, k) \tag{35}$$

where $\mathrm{u} = \mathrm{sn}^{-1}x = \int_0^x \frac{dt}{\sqrt{(1-t^2)(1-k^2t^2)}}$, Jacobi elliptic function, $\mathrm{m} = \frac{K}{l} = \frac{K'}{l'}$ k is chosen by $\frac{\mathrm{K}'}{\mathrm{K}} = \frac{l'}{l}$ relation,

$$K = \int_0^1 \frac{dt}{\sqrt{(1-t^2)(1-k^2t^2)}}, K' = \int_0^1 \frac{dt}{\sqrt{(1-t^2)(1-k'^2t^2)}}, \; k' = \sqrt{1-k^2} \tag{36}$$

Secondly, for matching the vertexes of micro resistor and its electrode, the transformation

$$\mathrm{u} = \frac{d-b}{b-a}\frac{t-a}{d-t} \tag{37}$$

was applied. Finally, inverse transformation of first step,

$$\mathrm{u} = \mathrm{sn}^2(\chi, \lambda), \frac{1}{\lambda^2} = \frac{d-b}{b-a}\frac{c-a}{d-t} \tag{38}$$

leads t-plane to χ-plane configuration, which easily calculates the geometrical resistance provided by the ratio of sides of rectangle $\frac{F}{F'}$ (Supplementary Figure 7d). If we non-dimensionalize the lengths as $X = l/l'$, $Y = a_{\mathrm{t}}/l'$, an excellent approximation of geometrical resistance was investigated with conditions $X << 1, Y < 0.5$.[6] The sensor's geometry and working circumstances satisfy above condition, we safely approximated the geometrical resistance as

$$\mathrm{G} \cong \mathrm{K}'(\mathrm{k})/\mathrm{K}(\mathrm{k}), \text{ where } \mathrm{k} \cong \tanh[(\frac{\pi}{2}\left(\frac{\mathrm{Y}}{\mathrm{X}}\right)]. \tag{39}$$

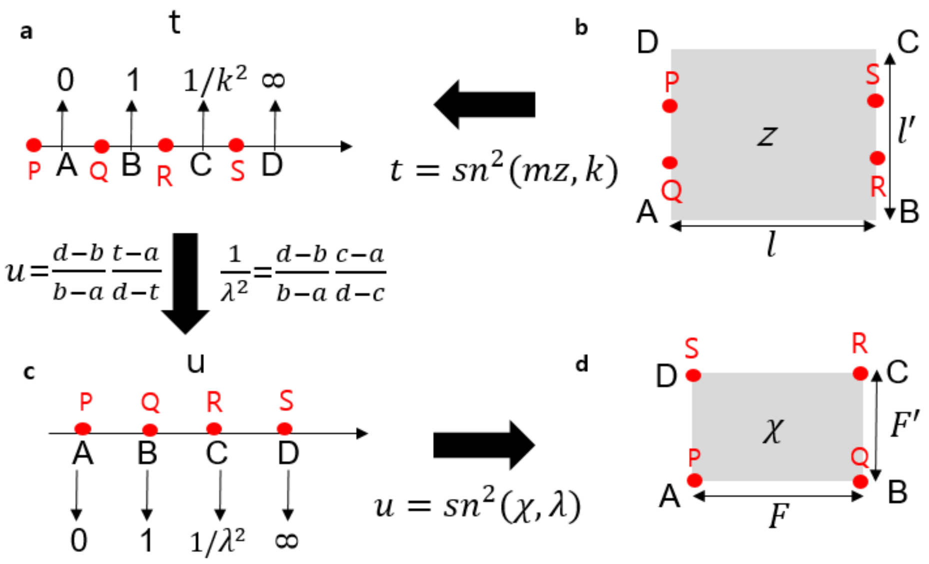

Figure 27. Three steps of conformal transformation, from Z-plane to χ-plane. a. t plane, each vertex is arranged along real axes, horizontal axes. b. Z-plane, geometrical representation of single micro resistor on imaginary plane. c. u-plane, vertexes of micro resistor and electrodes are matched together by t-u transformation. d. χ-plane, newly positioned vertexes of electrodes are merged to each four corners. The geometrical resistance can be calculated by using F,F^'.

4.5 Influence of AgNW quantity on sensor performance

As the nanowire is randomly distributed over the polymer, the NW composite could be treated as a continuous metal layer. Since the output signal of the sensor is related with the micro-scale contact between the NW composite and the corrugated electrode, the sensitivity and the electrical response will be maintained with the altered nanowire density. As shown in Figure 28a, the nanowire density was controlled in three different conductivity. Supplementary Figure 28b depicts that the output signals are identical to the theoretical value, which proves that the concentration is irrelevant to the electrical response. Yet, the low density of nanowires near the percolation threshold may have issues in stability and repeatability in signals.

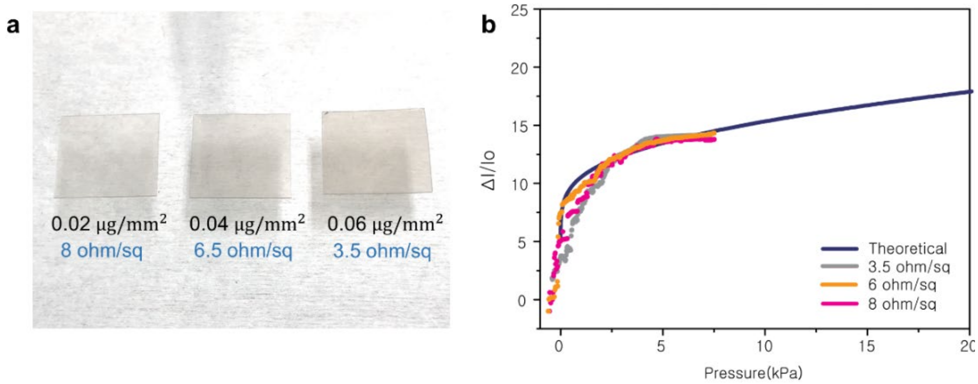

Figure 28. Output signal change with altering nanowire density a. Prepared nanowire composite with different density. b. Output signal with altering nanowire density.

4.6 Detailed information of laser sintered electrodes

Detailed information regarding laser sintering process is shown in Figure 29. Figure 29a depicts the TEM image of the nanoparticle ink with average diameter of 40 nm. Nanoparticle ink is spin-coated on PET in 200 rpm for 60 sec, and uniformly distributed nanoparticle layer is prepared as shown Figure 29b. The thickness of the spin-coated nanoparticle layer is around 1 μm as the SEM image is Supplementary Figure 29c. The magnified SEM image of the coated particles are shown in Figure 29d. The optical system for laser sintering fabrication is schematically shown in Figure 29e.

Flexibility of the electrode is shown in Supplementary Figure 14a, b. Ag microstructure is bent in 3mm curvature and the durability of the structure is shown in Figure 30b (5000 cycles in 1 Hz condition). The surface morphology of the Ag structure is captured in a larger view by the 3D surface profiler in order to investigate the uniformity of the structure (Figure 30c). Furthermore, the conductivity of the Ag microstructure is measured by the 4-point probe method. By the general relationship, $\rho/t = \frac{V}{I}\frac{\pi}{ln2}$, the conductance of the structure can be calculated by the measured resistance (V/I=0.0956 Ω) and the thickness of the Ag structure (t = 1 μm). The resultant conductance of the structure is therefore calculated by 2.32×10^{6} S m^{-1}.

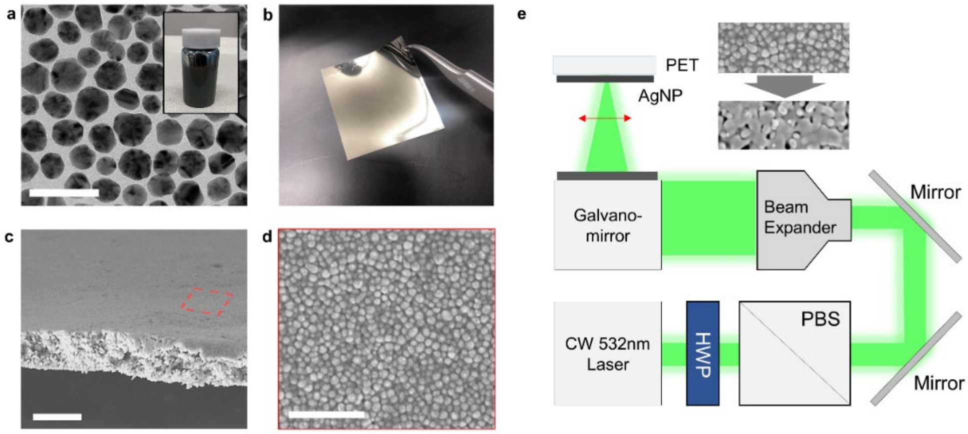

Figure 29. Basic information for laser sintering process. a. TEM image of Ag nanoparticle. Scale bar 100 nm. b. Picture of the spin-coated Ag nanoparticle layer on PET substrate. c. SEM image of the spin-coated layer. Scale bar 1 μm. d. Magnified SEM image of deposited particle layer. Scale bar 400 nm. e. Optical setting of the laser sintering system, where inset represents the melted particle after laser irradiation.

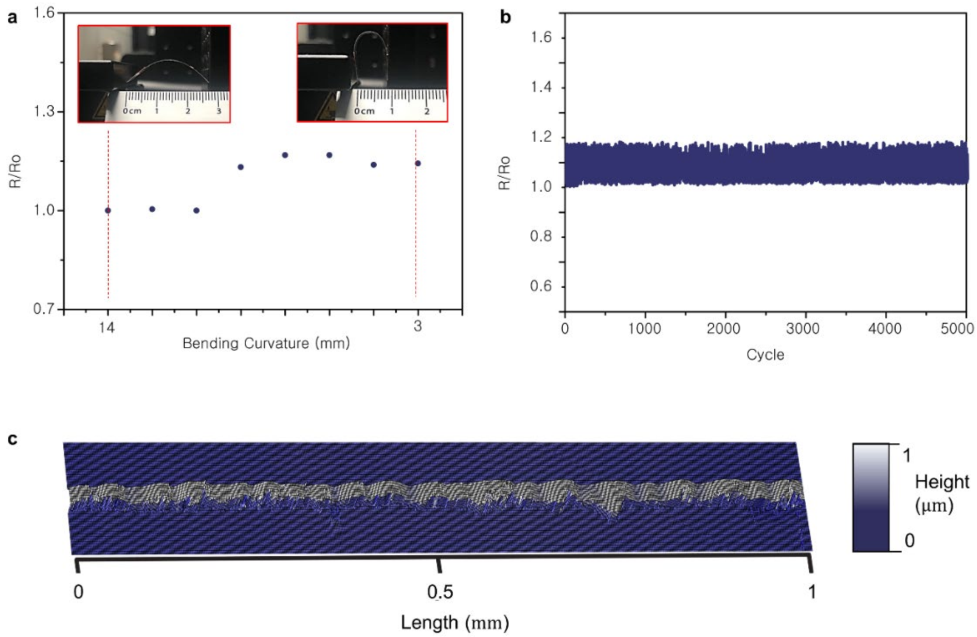

Figure 30. Flexibility and uniformity of the Ag electrode. a. Electrical stability under bending. b. Cyclic response under 3 mm bending curvature c. Uniformity of the corrugated structure

Chapter V

Laser-induced Crack of Metal Nanoparticles

5.1 Laser-induced crack generation

Selective laser sintering provides a sophisticated method for manipulating the critical crack strain. As illustrated in Figure 31, high power annealing lowers the porosity of the particle layer and provides a higher bonding energy per unit area, w_{f} through the necking between particles[34,35]. According to Irwin[36], a crack propagates further when the following condition is satisfied.

$$G_{\mathrm{c}} = -\frac{dU}{dA} = R \qquad (3)$$

where G_c is the critical energy release rate, U is the potential energy of body, A is the crack area, and R is the resistance function. The typical energy release rate for the displacement-controlled case gradually decreases with the crack size[37] as depicted in Figure 32. The resistance function, represented by the right-hand side of Equation 3 is defined as follows:

$$R(\mathrm{a}) = 2w_{\mathrm{f}}H(a - a_0) \tag{3}$$

where a is crack size, $H(x)$ is the Heaviside step function, and a_0 is the void size determined by the porosity of the sintered layer. Since critical cracking occurs at the intersection point of the *G* and *R* curve interpreting Equation 3, the resistance function is categorized into three cases based on the relative position of *G* to the maximum strain $\varepsilon_{\mathrm{max}}$; these include non-cracking (Figure 32a), stable cracking (Figure 32b), and unstable cracking (Figure 32c).

The excessive power of the laser anneals the particle layer into a fine bulk metal structure with high bonding energy. Since the *R* curve is above the set of *G* curves in Figure 32a, the intersection point is inexistent; thus, the crack cannot propagate further and maintains its initial size. We found that the condition for non-cracking was above ~13 mW. The illustration in Figure 32d and the SEM image demonstrate that the crack is restricted at the boundary of the annealed area, restricting cracking of the sensor's active area. Meanwhile, at low power annealing condition under 7 mW provides an inadequate bonding energy to bypass the envelope of *G* curves as shown in Figure 32c. In such a case, the *R* curve with bonding energy w_{f4} meets the *G* curve corresponding to some strain $\varepsilon_{\mathrm{c4}}$; however, the equilibrium crack size is infinitely large since the intersection point with maximum strain $\varepsilon_{\mathrm{max}}$ diverges. Moreover, the particle layer lacks the electrical path delivering sensor signals due to insufficient annealing power, and the corresponding crack feature is depicted in Figure 32f. The annealing condition between unstable cracking and non-cracking involves a distinct intersection point of the *G* and *R* curves throughout the straining range as shown in Figure 32b, with a finite equilibrium crack size for various conditions (stable cracking). In this condition, easy manipulating of the critical crack strain of the resultant structure is possible by varying the laser power. For instance, the higher power induces a smaller void size (a_2) and higher bonding energy (w_{f2}) on the structure, causing a smaller critical crack strain ($\varepsilon_{c2} < \varepsilon_{c3}$). We already confirmed such a relation in the interpretation. To investigate the dependence of the annealing power on the sensitivity in the stable crack regime, we found the correlation between the critical crack strain and the length of crack is given by:

$$\varepsilon_c^2 \sim \frac{4b}{L^2} p \tag{3}$$

where b is the thickness of the sensor, L is the length of the sensor, and p is the propagated length of the crack. Equation 5 shows that the square of the critical crack strain is proportional to the propagated length of the crack. As shown in Figure 32e, the crack is propagated with a certain crack length and reduces the conducting path of the sensor, which in turn, increases the resistance ratio α. Moreover, p directly represents the grain structure of the sintered area, whereas other properties like young's modulus are combined with other physical properties to define the grain size.

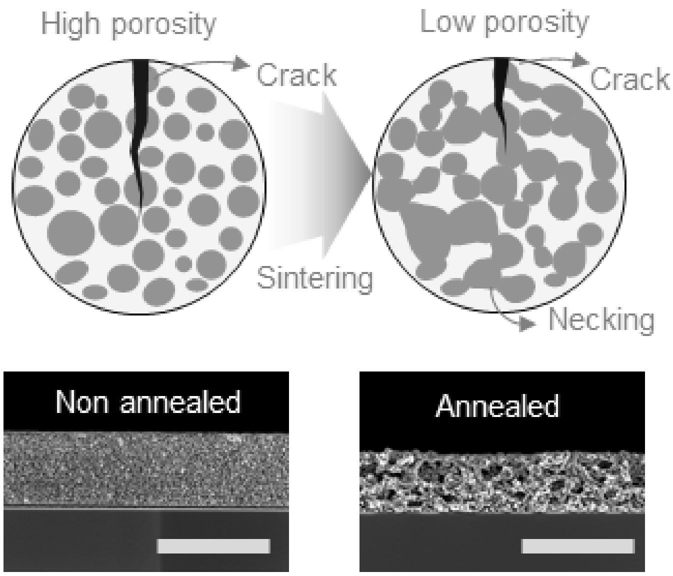

Figure 31. Schematic representation of sintered particle layer and SEM image of the cross section of annealed (right) and non-sintered (left) particle layer. Scale bar, 40 μm.

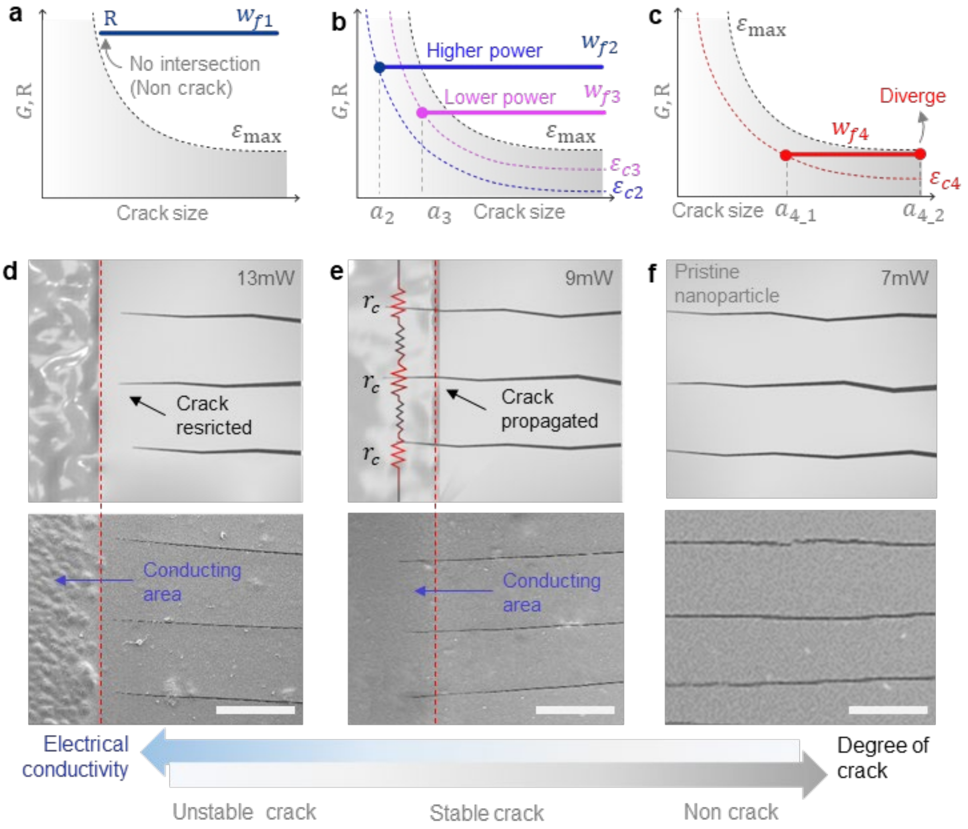

Figure 32. a-c Energy release rate curve and resistance function of 'Non-cracking' (a), 'Stable cracking (b), and 'Unstable cracking' (c). Arrow at the bottom describes the increasing direction of electrical conductivity (blue) and degree of crack (grey). d-f. Crack appearance for each regime, 'Non-cracking' (d), 'Stable cracking' (e), and 'Unstable cracking' (f). The first row indicates the schematic of crack length and the second shows the SEM images respect to each case. Scale bar, 14 μm.

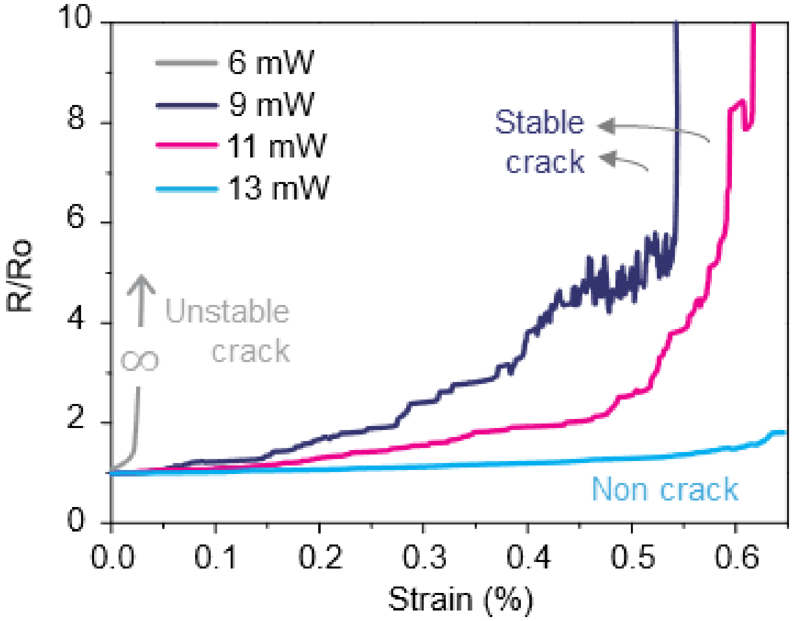

Figure 33. The operating output resistance of the sensors prepared by different laser power.

5.2 Highly sensitive strain sensor through crack-based structure

Previous works on crack-based ultra-sensitive sensors mainly involve fabrication by bending a metal-sputtered soft substrate[18-20]. The performance of the conventional sensors is engineered through varying substrate thicknesses, substrate modulus, annealing times, and using stress concentration structures[21-22]. However, previous approaches failed in deducing the relation between the control parameters and the sensor performance. The conventional technology barely explains the grain size that is associated with crack characteristics. A correlation between these can be examined by analyzing the signal outputs during the initial crack formation, whereas previous studies relied on the data obtained from the sample after cracking ends.

As depicted in Figure 34, initial cracking of the laser annealed layer is proceeded before utilizing as a sensor, and the electrical response in respect to strain in the cracking process significantly varies from that in the sensor operation process. The electrical resistance discontinuously increases in the initial micro cracking, whereas in the sensor utilization, a continuous change of resistance is observed since the gap of the crack is widened continuously. The discontinuous nature of initial cracking makes it difficult to obtain meaningful information from the signal output;

therefore, we designed a bending test under quasi-static conditions as shown in Figure 35, leading the set of discontinuous cracks to propagate continuously along the line. Crack occurs in regions where the local strain ε is higher than the critical crack strain ε_c (red), and do not occur below the critical strain (black). Since the first buckling mode of thin film is defined as a sinusoidal form, the curvature of the deformed sensor is represented as cosine curve.

The projected length of cracked zone l_{cp} is defined implicitly as follows:

$$\varepsilon\left(l_{\mathrm{cp}}, dl\right) = \varepsilon_c \tag{3}$$

where ε is the local strain of the sensor and *dl* is the displacement of the bending stage. The resistance ratio between the non-cracked and cracked region is defined as $\alpha = r_c/r_n$ where r_c is the resistance per unit length of the cracked zone and r_n is the resistance per unit length of the non-cracked zone. The normalized resistance of the sensor according to the displacement *dl* of the bending stage is expressed as:

$$\frac{R(dl)}{R_0} = \frac{2}{L}(\alpha - 1)l_{\mathrm{c}}(dl) + 1 \tag{3}$$

where R_0 is the initial resistance of the sensor and l_c is the length of cracked zone. In this model, two free factors, ε_c and α that determine the final shape of the electrical response are found by fitting the experimental data as shown in Figure 36. Higher laser power decreases the ε_c and α; $\varepsilon_c = 2.977 \times 10^{-4}, \alpha = 1.846$ for 9 mW, $\varepsilon_c = 2.4 \times 10^{-4}, \alpha = 1.4$ for 11 mW. Conditions under 6 mW are not enough to provide electrical pass ways through annealing between the particles and cases above 13 mW cannot be appropriately fitted by two free factors. A structure with larger grain size yields longer p and smaller crack asperity since the formation of the crack scatters less at the coarse grain boundary[38]. Moreover, the distribution of the crack asperity exhibits fractal similarity to the grain size distribution by the renormalization theory. Since the finely cracked face responds sensitively under strain, the sensor with larger p is more sensitive (Gauge Factor (GF) > 2000 at 0.55%) as shown in Figure 33. The overall process of the theoretical analysis is summarized in Figure 37.

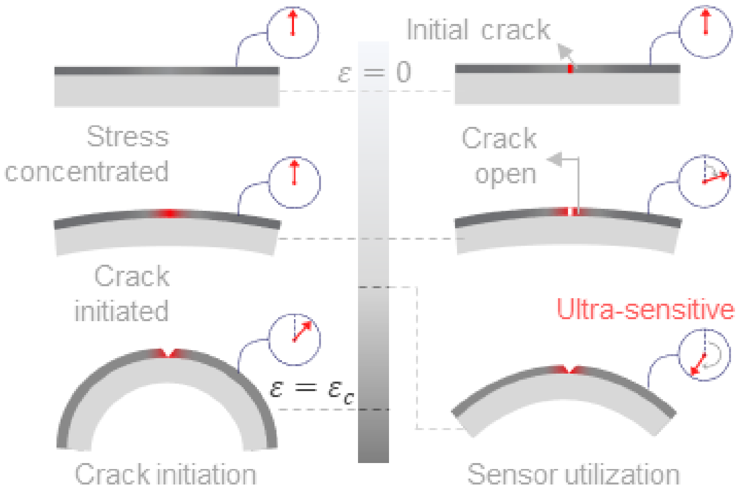

Figure 34. Electrical response while initial cracking (left) and sensor operation (right).

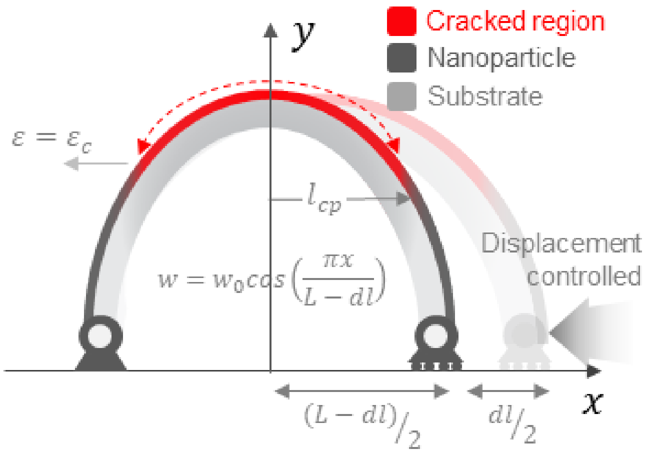

Figure 35. Schematic illustration and modeling parameters of displacement controlled bending environment.

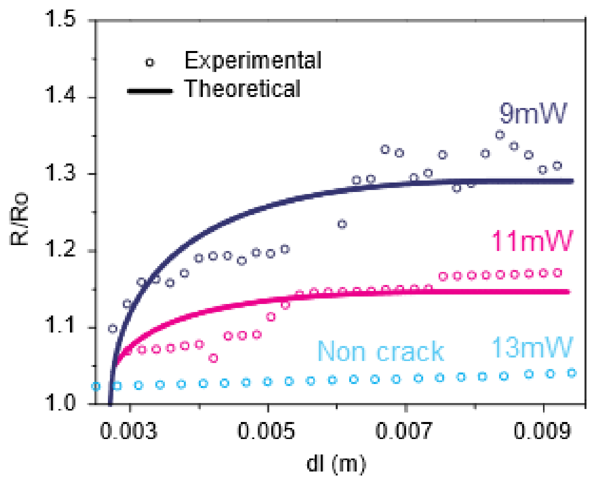

Figure 36. The initial cracking resistance changes of the sensors prepared by different laser power with model-fitting curve.

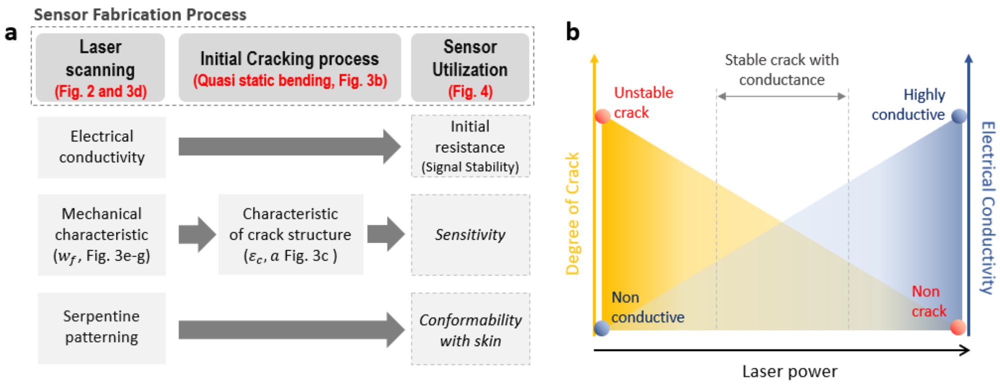

Figure 37. Main performance indicators during the fabrication process. a. Influence of laser condition on the parameters. b. Relation between laser power and the parameters.

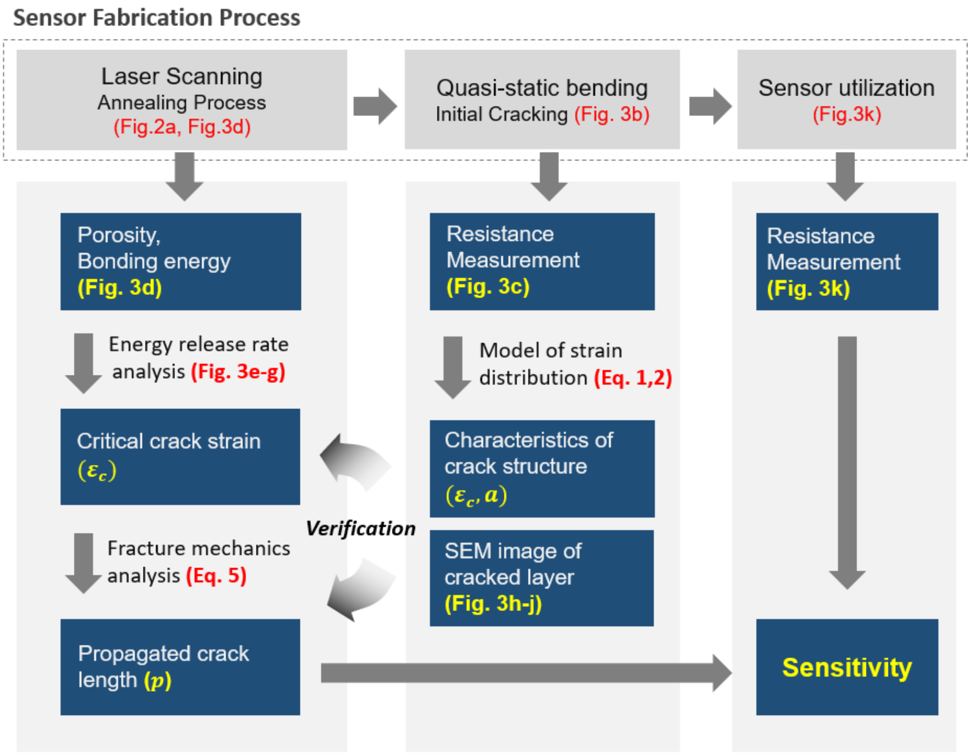

Figure 38. Theoretical analysis defining sensor's sensitivity

5.3 Geometrical modeling of the quasi-static bending condition to exploit crack characteristics

The porous sintered region of the sensor under quasi-static bending condition should be cracked locally when local strain exceeds above critical crack strain, ε_c. The situation is schematically illustrated in Figure 39, the red zone depicts a cracked region whose local strain exceeds the critical crack strain, *dl* is linear displacement of bending stage, and l_{cp} is the projected length of cracked zone, and *L* is the initial length of the sensor. Since the first buckling mode of beam is sinusoidal[1], the sensor would bend along sinusoidal curve. Therefore, the shape of bent sensor can be modeled as,

$$w(x) = w_0 \cos\left(\frac{\pi x}{L - dl}\right) \tag{1}$$

The sensor attached to the substrate (PET, thickness = 10 μm) conformably, the local strain of upper face of cosine curve could be directly read as the sensor's local strain. The height of cosine is defined using geometrical restriction, constant length condition,

$$\int_0^{(L-dl)/2} w_0 \cos\left(\frac{\pi x}{L - dl}\right) \mathrm{d}x = \frac{L}{2} \tag{2}$$

Such a constriction yields the w_0 as the function of *dl*. From elemental calculus, we could derive the local strain of the sensor as the function of *x* and *dl*.

$$\varepsilon(x, dl) = \frac{h\,\pi^2 w_0(dl)\cos\left(\frac{\pi x}{L - dl}\right)}{2(L - dl)^2\left(1 + \left(\frac{\pi w_0(dl)}{L - dl}\sin\left(\frac{\pi x}{L - dl}\right)\right)^2\right)^{\frac{3}{2}}} \quad (3)$$

where h is the thickness of sample. The curvature of cosine which decreases monotonically along x direction leads same trend of its local strain. Therefore, we can divide the cosine curve in two sections; the black zone: the local strain is lower than critical crack strain and the red zone: the local strain is higher than critical crack strain.

The projected length of cracked zone divides the cracked and the non-cracked zone and is defined as following implicit form.

$$\varepsilon\left(l_{\mathrm{cp}}, dl\right) = \varepsilon_c \quad (4)$$

In a given critical crack strain, the projected length of cracked zone is function of *dl* and monotonically increases.

To observe the microscopic phenomena of cracking, we conducted a quasi-static bending experiment with simultaneously measuring the electrical resistance of the sensor. The modeled electrical resistance can be expressed using projected length of cracked zone and resistances per unit length, r_c, r_n. A resistance variation after cracking should be negligible since initial cracking process is occurred discontinuously. When crack propagates beyond the initial void size slightly, the percolation of the electrical path could be broken. Such a change of physical parameter related to percolation probability around the percolation threshold significantly effects on resultant values[2] and we can treat each resistance as constant.

$$r(x) = \begin{cases} r_c \; for \; x|\varepsilon(x,dl) > \varepsilon_c \leftrightarrow x < l_{cp} \\ \\ r_n \; for \; x|\varepsilon(x,dl) < \varepsilon_c \leftrightarrow x > l_{cp} \end{cases} \tag{5}$$

Therefore, the total resistance of the sensor is deduced as,

$$R(dl) = 2r_c l_c + r_n(L - 2l_c) \tag{6}$$

$$l_c = \int_0^{l_{\mathrm{cp}}} \sqrt{1 + w(x)^2} dx \tag{7}$$

where l_c is length of cracked zone. **Equation 6** can be manipulated further

$$\frac{R}{R_0} = \frac{2}{L}(\alpha - 1)l_c + 1 \tag{8}$$

where $R_0 = r_n L$, initial resistance of the sensor, and $\alpha = r_c/r_n$, the resistance ratio between cracked and non-cracked zone. Combining **equation 4, 7, and 8**, we successfully found the relationship of the linear deformation of bending stage and the sensor's resistance. There are only two free factors in the model, the critical crack strain, ε_c and the resistance ratio α. Our purpose of designing the quasi-static bending experiment was exploiting the characteristic of cracking process which is hidden behind the data. The model naturally provides the effective factor determining the sensor's performance, two free factors ε_c and α. In order to find the two characteristic factors corresponding the laser condition, we employed the least square regression to fit the experimental dl *vs.* R/R_0 data using ε_c and α. The data were well fitted; however, actual signal had some jump point inferring the discontinuous generation of micro cracks. The model stands on the assumption of continuous propagation of cracked zone.

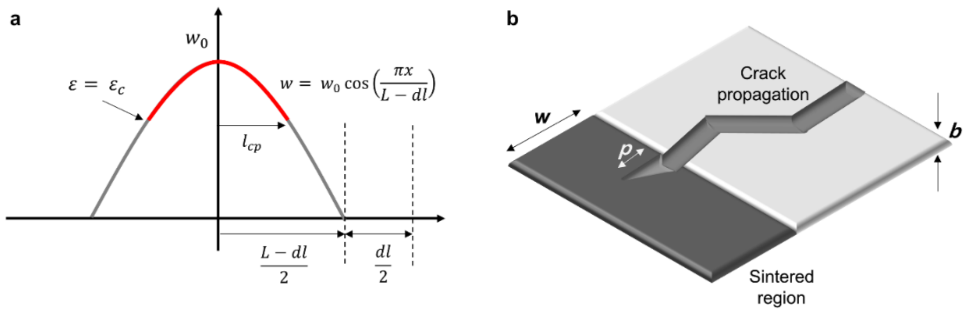

Figure 39. The modeling parameters related to a. the geometrical model and b. the thin film cracking model

5.4 Critical strain and propagated length of crack

When bending stress is applied to the as-prepared sensor, crack propagates from non-sintered to sintered region.

If a specific strain is applied to the conducting region, the crack in the non-sintered region will act as a crack seed in the sintered region, which will propagate the crack further. The relationship between crack depth and critical strain is essential to extract the performance characteristics of the sensor along with test. According to Irwin, cracks are known to propagate under the following conditions.

$$G_c = -\frac{dU}{dA} = 2w_{\mathrm{f}} \tag{9}$$

where G_c is the critical energy release rate, U is potential energy of body, A is crack area, and w_{f} is fracture energy per unit area. Since total strain energy is potential energy plus work done by external stress, the potential energy of elastic body can be defined as follows.

$$U = S - W \tag{10}$$

Since the experiment illustrated at Figure 35 was conducted under quasi-static displacement equilibrium bending condition, work done by external force, W can be expressed by

$$W = Pl \tag{11}$$

Also, elastic strain energy S should be calculated by

$$S = \int_0^l P dx = \frac{Pl}{2} \tag{12}$$

where P is external force, and l is linear deformation. Therefore,

$$U = -\frac{Pl}{2} = -S \tag{13}$$

The energy release rate related to quasi-static displacement equilibrium condition is defined as follows.

$$G = \frac{1}{b}\left(\frac{dS}{dp}\right)_l = \frac{l}{2b}\left(\frac{dP}{dp}\right)_l \tag{14}$$

where b is thickness of the sensor, and p is the propagated length of crack. We manipulated **Equation 14** further for exploiting the relation between critical crack strain and crack depth. Considering the geometry of the sensor system, the energy release rate can be transformed,

$$G = \frac{L\varepsilon}{2b}\left(\frac{d(E\varepsilon wb)}{dp}\right)_l = \frac{EwL}{2}\left(\varepsilon\frac{d\varepsilon}{dp}\right)_l \tag{15}$$

where E is young's modulus of sintered region, w is width, and L is length of sintered region. Inserting the energy release rate (**Equation 15**) to the critical condition occurring the cracking (**Equation 9**), the following relation is satisfied.

$$\frac{EwL}{2}\left(\varepsilon\frac{d\varepsilon}{dp}\right)_{\varepsilon=\varepsilon_c} = 2w_{\mathrm{f}} \tag{16}$$

We integrated the **Equation 16** both side with respect to p approximating that the bonding energy w_{f} is constant[4], and the initial strain-free state has no distinctive crack.

$$\varepsilon_c^2 = \frac{8w_{\mathrm{f}}}{EwL}p \tag{17}$$

Meanwhile, the fracture energy could be approximated by the atomic potential U_a with Taylor expansion about an equilibrium position

$$w_{\mathrm{f}} \sim \frac{1}{2\delta^2}\delta^2\left(\frac{\partial^2 U_a}{\partial r^2}\right)_{r=r_0} = \frac{1}{2}\left(\frac{\partial^2 U_a}{\partial r^2}\right)_{r=r_0} \tag{18}$$

where δ is displacement to occur a cracking of body, r_0 is equilibrium position of atom, and r is elongation coordinate. Young's modulus can be also approximated by similar way,

$$E = \frac{dP}{dr}\frac{L}{wb} \sim \left(\frac{\partial^2 U_a}{\partial r^2}\right)_{r=r_0}\frac{L}{wb} \tag{19}$$

With above ingredients, we have the approximated relation between critical crack strain and crack depth for the tiny strain regime of a thin film,

$$\varepsilon_c^2 \sim \frac{4b}{L^2}p \tag{20}$$

The scaling comparison leads the order of magnitude of the critical crack strain using the sintered region's geometry,

$p \sim O(10^{-7}\mathrm{m}), b \sim O(10^{-6}\mathrm{m}), \text{and } L \sim O(10^{-3}\mathrm{m}).$

$$\varepsilon_c \sim O\left(\frac{10^{-6}10^{-7}}{10^{-6}}\right)^{\frac{1}{2}} = O(10^{-3}{\sim}10^{-4}) \tag{21}$$

We could confirm the validity of **Equation 20** through the result indicated. The characteristics of cracking were calculated by the method found; $\varepsilon_c = 2.977 \times 10^{-4}, \alpha = 1.846$ for 9 mW, $\varepsilon_c = 2.40 \times 10^{-4}, \alpha = 1.4$ for 11 mW. The order of magnitude of the critical strain ε_c is 10^{-4} for each case which is good agreement with **Equation 21**. Furthermore, if we assumed that the resistance ratio α is linearly proportional to the length of crack,

$$\left.\frac{\varepsilon_c^2}{\alpha}\right]_{\mathrm{power=11\,mW}} = 4.80 \times 10^{-8} \sim \left.\frac{\varepsilon_c^2}{\alpha}\right]_{\mathrm{power=9\,mW}} = 4.11 \times 10^{-8} \tag{22}$$

Since we fabricated the sensors maintaining the same geometry, above quantity should be similar for varying the laser power. Note that the independent approach to investigate the crack characteristics merged in **Equation 4 and 20**.

5.5 The relation between crack asperity and the sensitivity

Kang *et. al.*[5] found that the crack asperity distribution has fractal self-similarity to the grain size distribution by renormalization group theory. They brought the log-normal distribution which is well explained grain size distribution. The key fitting parameters are the grain size parameter ε_0 and the deviation μ. Defining the log-normal distribution as crack asperity distribution, they derived the normalized conductance S with respect to the strain ε.

$$S = \frac{1}{2}(1 - \mathrm{erf}\left(\frac{\ln(\varepsilon/\varepsilon_0)}{\mu}\right)) \tag{23}$$

where erf(x) is the error function, ε_0 is grain size parameter, and μ is the deviation of distribution. As shown in Figure 40, the sensor data is fitted by Equation 23, and found the large grained structure has higher sensitivity. (ε_0 = 0.2489, $\mu = $ 1.196 for 6 mW, ε_0 = 0.38, $\mu = $ 1 for 9 mW). Note that the actual grain size ($d_0 = k\varepsilon_0$) cannot be directly defined by the grain size parameter (ε_0), since the parameter k differs by the laser power.

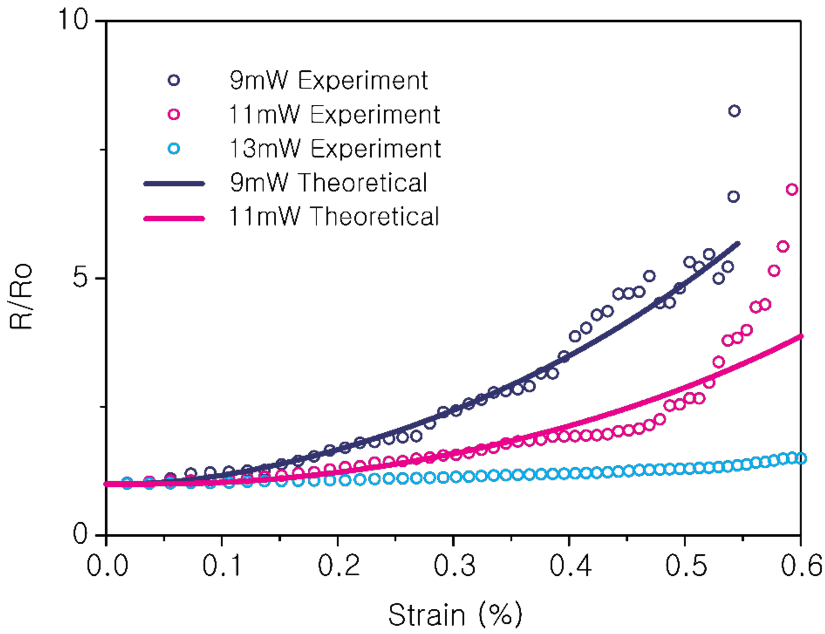

Figure 40. Output signal variance among different laser power conditions

Chapter VI

Deep-learned skin decoding human motions

6.1 Highly sensitive skin-like sensor fabrication

The process requires a sensor that is sensitive enough to measure the minute deformation while holding high conformability with the skin in order to catch the subtle topology transitions of the wrist. Digital laser fabrication provides a viable solution to obtain both features through laser controlled cracking and serpentine patterning. The periodic serpentine structure exhibits higher level of elastic deformation, causing a conformal contact between the electrode and skin; this promotes sensing of minute skin deformation. A crack-induced layer with micro serpentine patterns can easily be generated by simply scanning the laser with different power conditions. Cracked layer is used as a sensing element, since these structures are widely utilized in detection of minute mechanical stimulations. Figure 41 illustrates the fabrication process and the structure of the sensor. Colorless Polyimide (CPI) is uniformly coated on a glass substrate and fabricated silver nanoparticle (AgNP) ink is then spin-coated over the layer. The bilayer of AgNP and PI is firstly patterned into the serpentine structure through a 355 nm wavelength laser ablation (over 100 mW). This process is better than the conventional fabrication method[29,30] often requiring high temperature, vacuum environment, or a pre-processed mold. Subsequently, the laser power is lowered within a certain range (6 mW ~ 13 mW) to selectively convert the AgNPs into a crack-induced layer. The patterned structure is easily peeled from the glass substrate, with Figure 42a depicting the magnified optical image of the final structure. The sensor performance is controlled through the annealing region as depicted in the middle line of Figure 42b. The fabricated free-standing sensor is displayed in Figure 42c.

The sensor is directly mounted on the skin through the assistance of adhesive PDMS. The strain distribution of the sensor under 15 % strain is observed through a finite element method (FEM, COMSOL Multiphysics) as illustrated in Figure 42d. On account of the out-of-plane buckling deformation of the sensor, an effective strain under 2% is applied through the electrode.

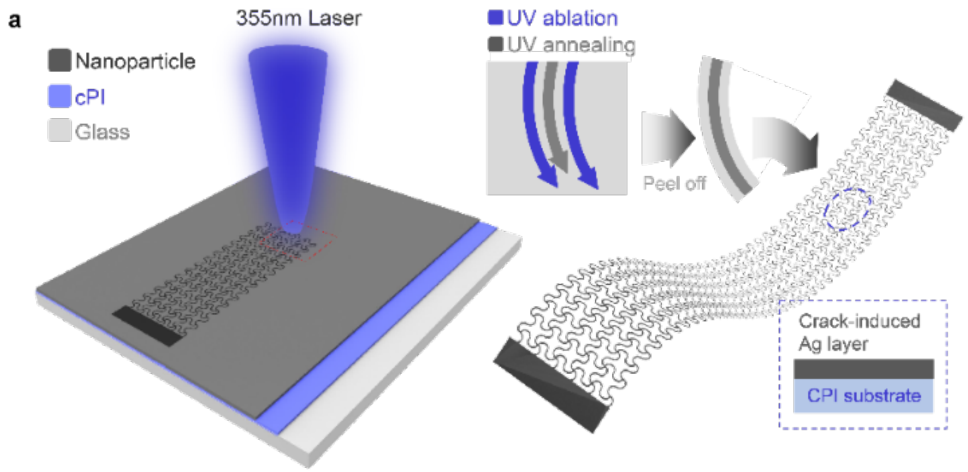

Figure 41. Highly sensitive skin sensor fabrication by laser induced crack generation. a, Schematic depicting the patterning and crack fabrication by laser fabrication.

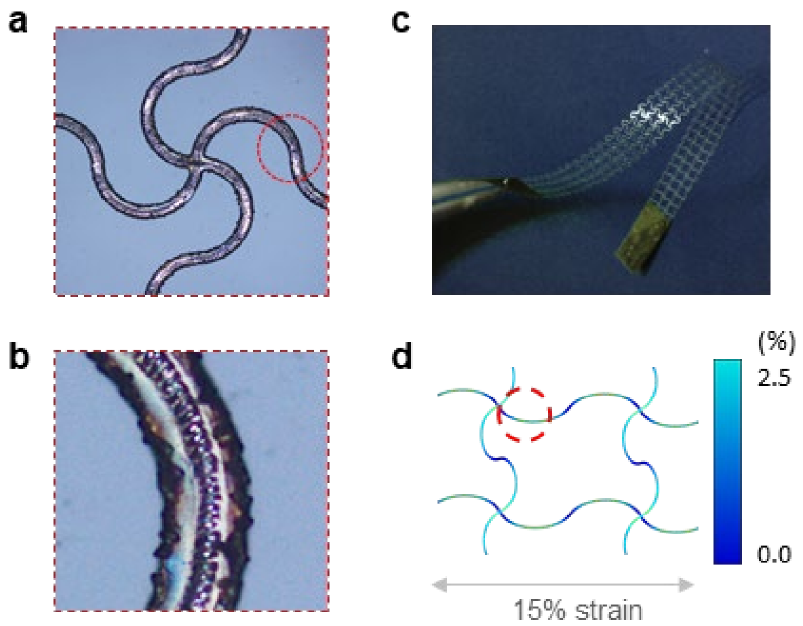

Figure 42. a, Optical image of the fabricated sensor. Scale bar, 200 μm b, Magnified image of the sensor which distinctively shows the annealed region. Scale bar, 50 μm c, Picture of the free-standing fabricated sensor. d, FEM image showing strain distribution of the sensor.

6.2 Deep-learned skin-like sensor system

An illustration of motions in human body is shown in Figure 43. Movement of any joint is associated to its surroundings[10], involving electrical signals such as action potential of muscle, or mechanical signals of skin deformation. The blue arrows highlight the likely information flow caused by the movement from the main joints. Attempts to capture these signals are numerous including measuring the movement of the foot from shin[11], knee movements from thigh[12], and information converging around the pelvis[13] with signals representing the entire gait motions. Similarly, motion of the arm[14] and the face expression[15] can be also identified. Predicting the status of motion aside from the main joints is like earthquake prediction, mainly involving time, location, and magnitude. Similarly, the aim of our study is to decode and extract the 'epicentral' motions from the detected signal. Among the numerous motions generated in the human body, hand exhibits the highest degree of freedom which exquisitely performs a range of tasks[16]; hence, predicting its motions is very challenging. Our study, therefore, initially focused on decoding the dynamic finger motions in real-time. Figure 44a illustrates the platform of the sensing system. A topographical movement of the wrist is triggered by the epicentral finger motion, with the attached crack-based sensor producing a signal containing the motion information. A sample scanned electron microscopy (SEM) image of the sensor crack is shown in the lower right corner. The magnified image of the sensor attached above the skin is shown in Figure 44b. The serpentine patterns allow a conformal contact with the epidermis, enabling a more direct measurement of skin deformation. The design of our analysis is shown in Figure 44**c**. The wrist contains information reflective of several finger motions. The highly sensitive crack-based sensor detects the deformation of the wrist as unidentified signals. The signals are then analyzed in a temporal sequence through our encoding network, and the current status of the motion is simultaneously generated through the decoding network.

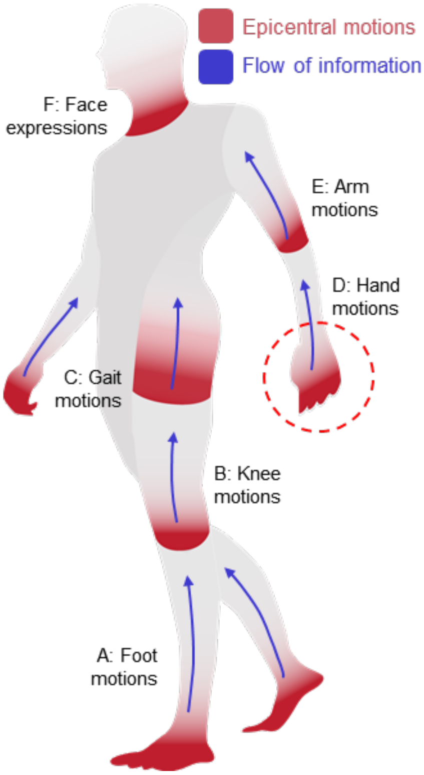

Figure 43. Schematic depicting the possible flow of information through our body. The information may include foot, knee, hand, arm, gait, and also face expressions.

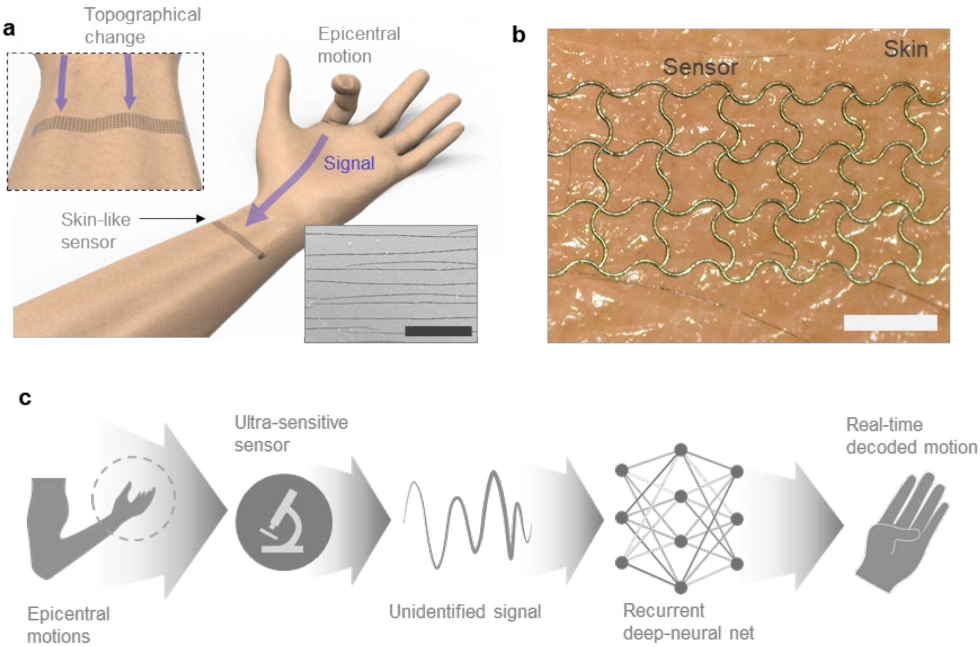

Figure 44. a, Illustration of measuring the epicentral motions of fingers. Upper left image depicts the measurement of the topographical change of the wrist caused by the finger motions. Lower right image shows the SEM image of the cracked region of the sensor. Scale bar, 40 μm. b, Magnified image of the sensor conformably attached on skin. Scale bar, 1 mm. c, Design of the proposed sensory system.

6.3 Learning the dynamic motions with a single sensor

We used a deep neural network to identify complex hand motion from highly sensitive sensor signals. As illustrated in Figure 45, various hand motions result in signals from skin deformations and muscle movements. To guide our network to correctly identify the moving finger, we defined a metric space as in Figure 46. The R values express the bend of a finger while θ values represent the identity of the moving finger.

The metric is designed to consider the spatial positions of the fingers and how humans distinguish different hand motions. It is much harder to distinguish hand motions when the fingers are barely bent than when they are fully bent. Furthermore, the motions of two fingers apart are more easily distinguished than motions of two fingers that are close to each other. Therefore, to represent this, points on our metric space are closer to each other when r and the difference between their θ values are lower. This Euclidean distance between points is used as our network's loss function to help it learn to differentiate different hand motions. For example, if the little finger is the finger that is bent, we pose a higher penalty for our model when it incorrectly determines the bent finger as the thumb than when it incorrectly determines it as the ring finger.

Therefore, we designed neural network to accomplish two tasks: firstly, analyzing sensor signal patterns into a latent space encapsulating temporal sensor behavior and secondly, mapping latent vectors to our finger motion metric space defined above. Encoding and decoding network in Figure 47 achieve above goals respectively. To maximize user convenience regarding usability and mobility, we used a single-channeled sensor to generate signals corresponding to complex hand motions. Thus, it was necessary to utilize temporal sensor patterns to correctly determine the hand motion the signals were generated from. We therefore trained a long short-term memory (LSTM) network, a type of RNN architecture, to identify such temporal behaviors, as it is a type of deep neural network designed to analyze sequential data. To map latent vectors into corresponding points in our 2d metric space, the decoding network is composed of two separate dense layers, mapping encoded latent vectors into r and θ respectively.

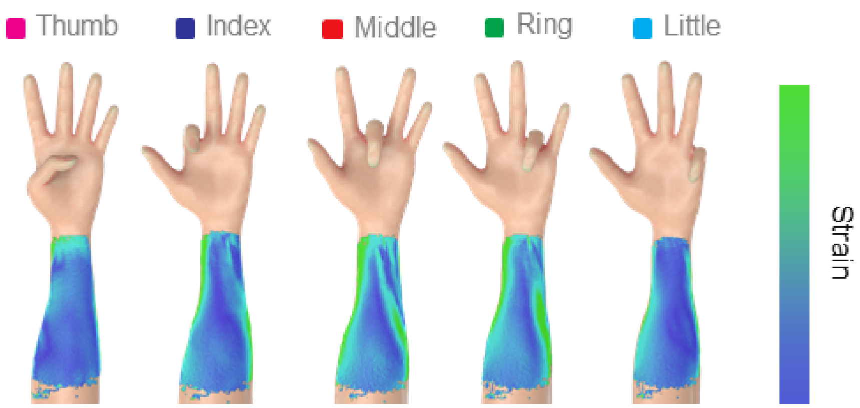

Figure 45. Depiction of skin deformations for different finger bending motions.

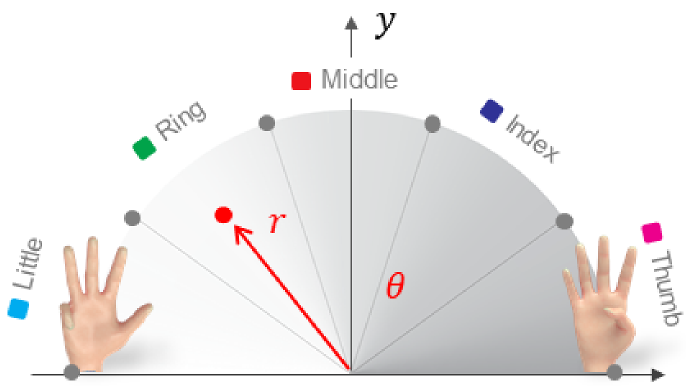

Figure 46. Metric space defining single finger bending motions: physical alignment of fingers in a hand is expressed in the metric space with R representing the amount of a finger bent and θ identifying the position of a finger in a hand.

The resulting vectors from our network are visualized in Figure 48. We used principal component analysis to project the latent vectors onto the 2D vector space. In general, the sensor signals corresponding to a specific finger create a circle in the 2D vector space. Since the finger motions involve a cycle of bending and unbending the finger between a starting straightened position and an ending bent position, this observation is expected. However, there are two main changes to the data after it is passed through the encoding network. Firstly, the starting points, where all fingers are straightened, are aligned by the encoding network. By labeling the input vectors as a point in the half-circle metric space that we defined, we intended to represent the starting points as closer vectors in our metric space. The alignment above demonstrates that our model maps straightened finger motions to closer latent vectors as we intended. Secondly, the data points for the ring finger, which were widely distributed across the projected 2D plane before encoding, create a circle with a radius similar to those of the other fingers after encoding. The encoding network transforms different data points to latent vectors that represent their corresponding finger motion. Therefore, even if the original sensor signals had different values, they are still projected to similar latent variables as long as they correspond to the same finger motion. This demonstrates that our network correctly utilizes temporal sensor behavior to analyze the different patterns for each finger motion. Figure 48 shows the generation of r and θ values by the dense layers from the network-produced vectors mapped to the metric space. Even though some data points are misclassified when the r value is low, dense layers clearly discriminate different finger motions when the fingers are significantly bent and the r values are high (Figure 55). A real-time demo of our network analyzing sensor signals from the hand motions of the sensor wearer can be seen in Figure 50.

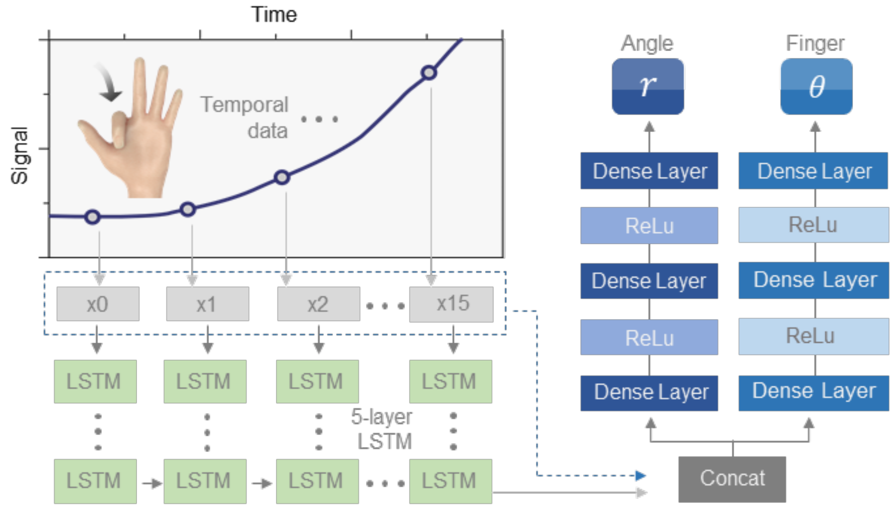

Figure 47. Neural network is composed of an encoding network and a decoding network. LSTM layers are used in encoding network to analyze temporal sensor patterns to generate latent vectors. Two independent dense layers map created latent vectors to our metric space expressing hand motions. Dropout is used as the regularization technique to prevent the network to be overfitted to a single use case.

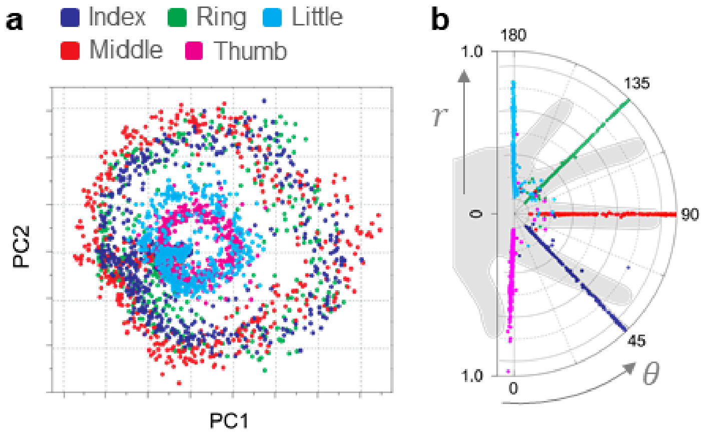

Figure 48. 2D PCA illustration of output vectors produced by encoding network. Each circular cluster demonstrates that encoding network can correctly identify cyclic finger motions from sequential sensor inputs. e Figure of how sensor inputs in training dataset are mapped to the metric space after passing our network

Finger motions are generated by analyzing the strain changes at the subject's wrist site. However, a simple wrist movement can also modify sensor signals by producing non-finger motion noises. To verify whether our sensor can generate signals that allow our model to distinguish between different noises and finger motions, we conducted an additional experiment to check if our model can classify five motions and three types of noises generated by non-finger bending motions as shown in Figure 49a. Three noises are sensor signals caused by directly touching the sensor, twisting the wrist, and bending the wrist, we call them touch, twist and wrist respectively.

To perform the classification task, we modified the decoding network to a 3-layered dense block producing 8-dimensional vector output. Each value in an output vector is model predicted probability for each 8 classes. A class with a maximum probability is chosen as the model predicted class for a given sensor input. As illustrated in the confusion matrix in Figure 49b, our model could correctly classify finger motions and noises with 96.2% in average and 92.9% in the worst case for little finger motions. The result shows that our sensor can generate distinctive signal patterns for different hand motions including non-finger motions so that our model can distinguish finger motions from noises generated by three non-finger motions.

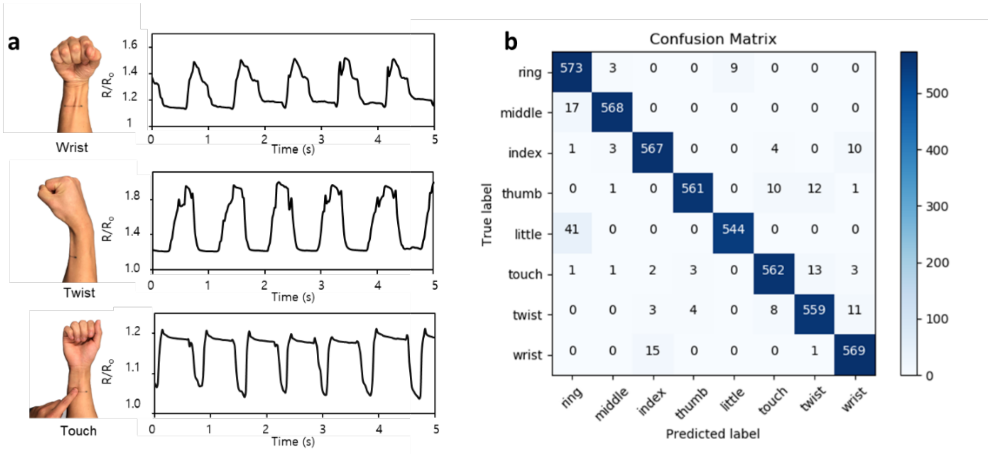

Figure 49. Noise analysis of the sensor a. Signal outputs of various noise. b. Confusion matrix of decoding finger motions included with external noise.

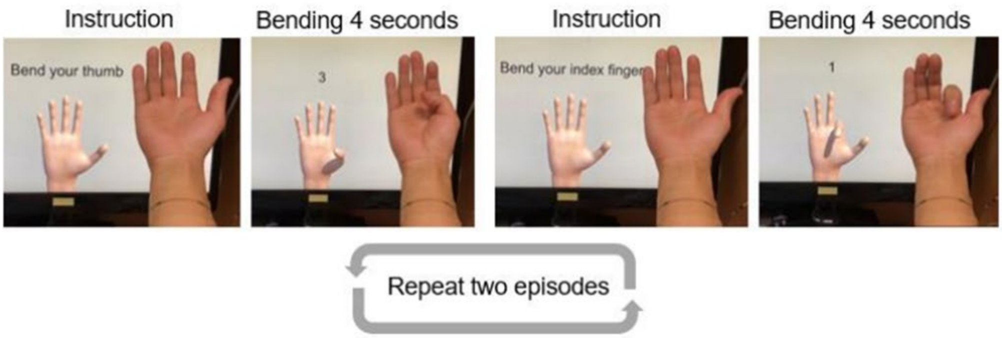

Figure 50. Snapshot of user following the instructions

From the above results, we know that given the sensor data of a user, our network is trained to correctly classify the user's finger motions. However, attaching the sensor to a different user, the muscle movements and sensor values corresponding to the hand motions of the new user may be different from those of the previous users, as human muscle movement vary from person to person. Since our network is trained for different sensor patterned dataset, the network may consequently fail to determine hand motions by the new user. We therefore need to retrain the network with the new data from the new user. However, if we train our model from scratch, we need at least 2000 sensor frame from 80 seconds of finger movement for each finger. It is impractical and inconvenient to collect a 400 seconds of training dataset each time the sensor is attached to a new user. Even if we were to collect enough data, the training time necessary for the LSTM network to extract the hidden sensor patterns from the dataset is too high. Similar issues arise when the sensor is attached to an area different from before or when the sensor itself is replaced with a new one. These problems hinder practical applications aimed for usage by multiple end users.

To address these problems, we designed the RSL (Figure 51), a deep learning system guides user to collect data and automatically processes them to retrain our models with only a small amount of data in a short period of time. The procedure of the system (Figure 50) involves following onscreen instructions to collect data for 8 seconds per finger when the sensor is placed on a new user . By sliding a time window of size 16, we group the collected data to form 16 consecutive sensor signal input. The generated input is used as a single input for our model.

The RSL system uses transfer learning[42] techniques to utilize knowledge on sensor behaviors obtained during previous training steps. The parameters for the LSTM and dense layers are then transferred from the pre-trained model to the new model. After retraining for around five minutes with the newly collected data, the model is then ready to generate the hand motions of the new user.

Through RSL system, all steps required for generating the hand motions of a new user are processed automatically. Typically, the temporal behavior patterns of the sensor signals that were already previously analyzed by our pre-trained model is transmitted to the new network. Consequently, the retraining time is massively reduced because the network only needs to retrain its mapping functions to map input values to a different range of sensor values. The effectiveness of using transfer learning is evident in the loss comparison graph (Figure 53). In the absence of transfer learning, over 20 minutes are required for the loss to decrease to below 0.1, whereas in its presence, the time is within five minutes for the same dataset.

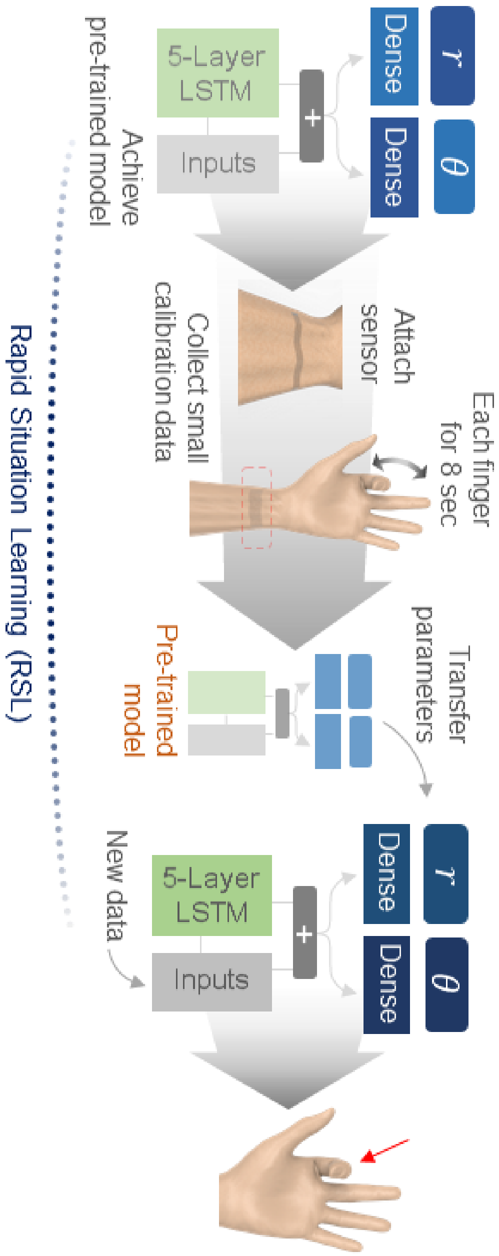

Figure 51. The processes of rapid situation learning (RSL) that utilizes transfer learning. When the sensor is attached to a new position and a small amount of retraining data is collected, the new network utilizes knowledge learned during pretraining by transferring parameters from pretrained network, reducing the amount of dataset, and time for retraining. g Photo of actual hand motion generation.

As a proof-of-concept demonstration of our system's expandability, the sensor is used to decode the keyboard typing of numpad which the signals are combined with the movements of the wrist and the finger. The modified model decoded 9 classes of number in real-time that are pressed by fingers (Figure 56). Moreover, a single sensor is also attached on pelvis to identify the gait motions. The modified model successfully generated the positions of the ankle and knee as shown in Figure 57. Moreover, the signals are collected in the cases where the wrist and the finger movements are coupled.

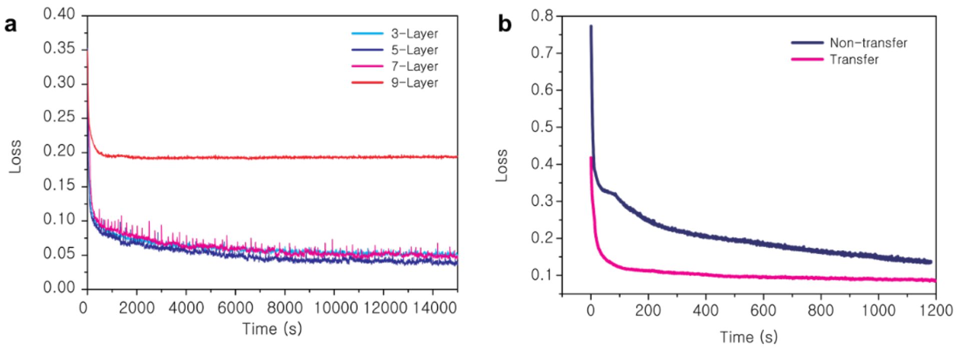

Figure 52. Learning characteristics. a. Varying LSTM layers and loss difference. b. Loss difference between non-transfer and transfer learning data.

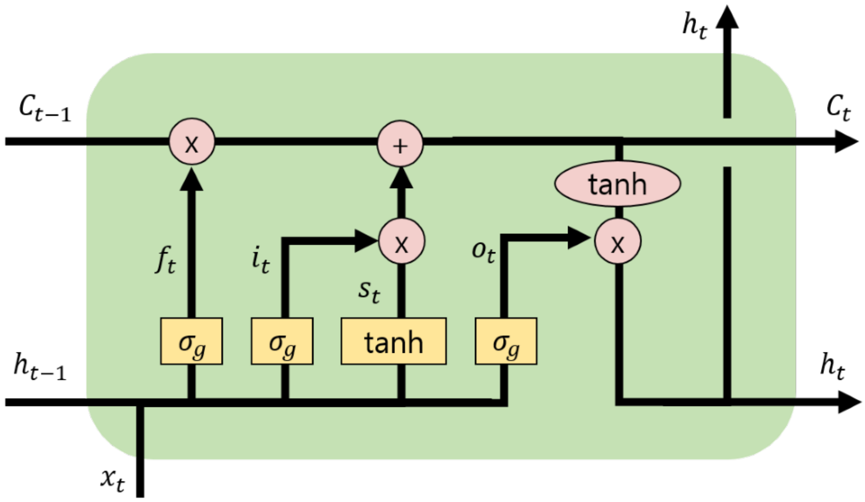

Figure 53. Structure of the LSTM unit

6.4 Data Processing and Network Design

Two datasets were used to train the model: a dataset for pre-training and a dataset for recalibration. The data values within the pre-training dataset (15930 frames) range from 170 to 195 (units). 3,186 frames were collected from 100 seconds of finger motion data for each finger. The recalibration dataset contains 1,000 data frames, or 200 data frames from 8 seconds of data for each finger. The data values within the recalibration dataset exhibit a different range, which is dependent on the position of the sensor, the user, and the sensor itself.

By using a sliding time window of size 16 along the data sequence, 16 frames of consecutive sensor values were regarded as a single input. This was done to utilize the temporal behaviors of the sensor signals. Each input was labeled with two float values, r and θ ($0 \leq r, \theta \leq 1$). θ represents the finger with which the movement is done. θ values start from 0 if the movement is from the thumb and ends at 1 if the movement is from the little finger, with the values for the fingers in between increasing linearly by 0.25.

For r, which represents how bent the finger is, we picked the local maximum and minimum of the sensor values to distinguish the bent and unbent states. Each local maximum and minimum were labeled as having an r value of 1 and 0, respectively. For intermediate sensor values, the r values were linearly interpolated as the ratio of the difference between the current sensor value and the closest local minimum and the difference between the closest local maximum and the closest local minimum.

Although we could have used a motion capture device or depth camera to be more precise with our r values, we decided to avoid such devices as we want a simple and convenient method to train our model with only our single-channeled sensors.

We then split the pre-training dataset into training and test subsets. By chronologically organizing and splitting the 16-frame-long inputs belonging to one data sequence into 10 consecutive groups of equal size and randomly choosing eight of those groups for the training set and two for the test set, we increased the regularization effect by minimizing the number of frames that appear in both the training set and the test set. This was done for all data sequences in the pre-training dataset. In both the training dataset and the test dataset, the same number of groups were selected for each finger to even out the data distribution.

Our network consists of a 5-layered LSTM network, a type of Recurrent neural network and two separate 3-layered dense networks. Recurrent neural network is a type of neural network typically designed for dealing with sequences of inputs. RNN is composed of RNN units which combine current input and hidden vector passed from previous unit to generate current output. Therefore, RNN is well-suited to processing time series data. Unlike standard RNNs, LSTM networks additionally train three gates (input gate, output gate, and a forget gate) to regulate the flow of information from one cell to another. The overall structure of the LSTM is illustrated in Figure 54**.**

LSTM unit takes an additional vector, C_{t-1}, the previous memory cell. Following its literal meaning, memory cell contains integrated information from previous LSTM units. LSTM has a forget gate, an input gate, an output gate inside each unit controlling the next memory cell, C_t, to be passed on to the next unit. Two activation functions, σ_g, for sigmoid function and tanh for hyperbolic tangent functions, are applied for each gate outputs to control the range of output vectors. Here's the overall equation of three gates vectors.

$$f_t = \sigma_g (W_{xf} x_t + W_{hf} h_{t-1} + b_f) \tag{24}$$

$$i_t = \sigma_g (W_{xi} x_t + W_{hi} h_{t-1} + b_i) \tag{25}$$

$$o_t = \sigma_g (W_{xo} x_t + W_{ho} h_{t-1} + b_o) \tag{26}$$

Three vectors, f_t, i_t, o_t, are parameterized by its corresponding weights matrices W. Weight matrices are trained so that the unit can modify memory cell based on current input and hidden vector. Taking current input vector, x_t, and hidden vector, h_{t-1}, as input, gates generate vectors ranging from 0 to 1. Sigmoid function, σ_g, is used to bind the gates vectors in between 0 and 1. However, they are multiplied to different vectors to achieve different purposes.

$$st = \tanh\left(Wxgxt + Whght-1 + bg\right) \quad (27)$$

$$Ct = ft \odot Ct-1 + it \odot st \quad (28)$$

$$ht = ot \odot \tanh(Ct) \quad (29)$$

Following its literal meaning, ft is multiplied element-wise to previous memory cell Ct−1 to determine how much information from the pass are going to be forgotten in current unit. Symbol ⊙ means Hadamard product, which also stands for element-wise product. Input gate vector it, in contrast, determines the amount of current input xt and ht−1 to be taken account in current memory cell Ct. Input gate vector, it, is multiplied by st and added to memory cell. st represents memory generated from current input and previous hidden state. Hyperbolic tangent is used to generate st so that not only the magnitude but also the sign of st is considered. Finally, Output gate vector is multiplied by the current memory state Ct to generate a new hidden state ht and it is passed to the next state. The last LSTM unit will take a memory cell containing key information summarizing passed input sequence and generate output based on it. Generated latent output vectors imply sensor patterns for sensor signals within a time window.

Since we aimed to not only accurately determine the hand motion but also quickly re-calibrate the sensor when needed, we determined the number of layers for each network by comparing testing accuracy versus training time as shown in Figure 53. A 5-layered LSTM network achieved the fastest training time to reach the same level of accuracy. However, 9-layered network shows significantly higher loss values than other shallower networks. While a deeper neural network can interpret more complex patterned data, it can also easily be overfitted for a bounded dataset. 9-layered network contains an excessive number of parameters so that it is too biased to training dataset. As a result, the network is overfitted to the training dataset so that it is not generalized to predict unseen data pattern. In particular, we are utilizing a sequence of a single sensor value to generate corresponding hand motion. Thus, our task has a relatively low data dimension. Furthermore, the data is collected manually by attaching it on human arms, making it difficult for us to collect huge amount of data. Thus, the LSTM with 3 to 7 layers were more suitable for our current dataset size, while 9-layered LSTM was too deep. This result can be changed if we collect more data from more people.

Each frame within a 16-frame-long input was sequentially passed into LSTM units to produce a 128-dimensional hidden vector. Three trainable gates in each LSTM unit controlled the information flow from a unit to the next unit, preventing the gradient vanishing problem and enriching the information received by dense layers. While LSTM layers could process sequential data inputs to generate latent vectors summarizing temporal behaviors of sensor signals, we are aiming to map such high dimensional latent vectors into our metric space expressing single-finger motions. Therefore, a decoding network that maps implicative latent vectors into coordinates in half-circle metric space is needed. Decoding network is composed of two separate dense layers. Dense layers allow our model to decide the dimension of output vectors while decoding information embedded in latent vectors from the encoding network.

The resulting 128-dimensional vector was concatenated with the input to create a 144-dimensional vector, which is then passed onto the decoding network consists of two separate dense layers groups. One generates r values while the other generates θ values. The rectified linear unit (ReLU) was used as the activation functions for the dense layers. To prevent overfitting to the small recalibration training dataset, 30% dropout was applied to all layers. We implemented the network using the PyTorch deep learning framework. The Adam optimizer of learning rate 10^-4 was used for training the network. The Euclidean distance between the predicted point and the labeled point within our metric system was calculated and used as the loss function for training our network.

To visualize the user’s hand motion for our real-time demo, a virtually generated hand that mirrors the user’s hand motion was generated using the cross-platform visual engine Unity (unity.com). We modified a VR hand motion asset in the Unity Asset Store to implement our demo. After a user attaches the sensor, our network generates r and θ values, which are then sent to our Unity application through socket connections and used to move the virtual hand in accordance with the values and the corresponding hand motion on the metric space we defined in Figure 48. Socket connections were created with the Python socket module API. For points labeled with a θ value that is not a multiple of 0.25, we projected the point to the nearest finger and moved the corresponding finger of the virtual hand. To avoid collisions caused by simultaneous hand motion orders, fixed time step that determines when physics calculations are performed in Unity is set as 0.3 seconds.

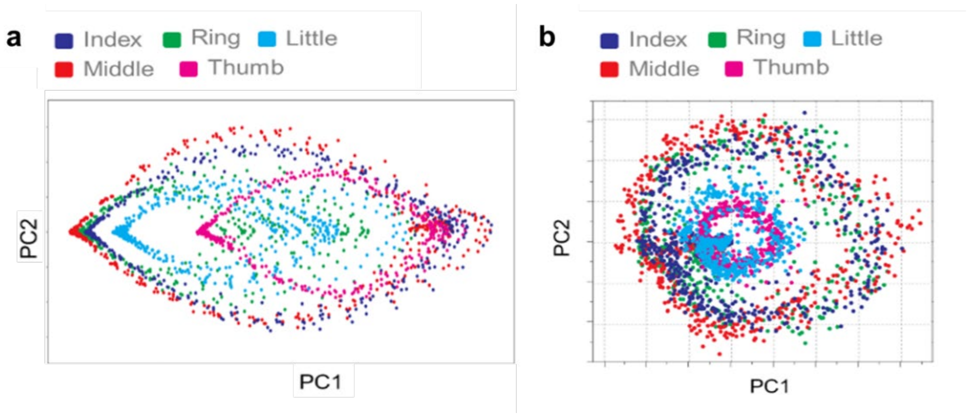

Figure 54. PCA analysis of sensor a. PCA before passing encoding network. b. PCA after passing encoding networks**.**

6.5 Keyboard typing

In addition, we collected sensor signals while typing number pad keyboard to demonstrate the use cases where wrist movements and finger movements are coupled. We collected 12000 sensor frames while typing a number keyboard. We again grouped 16 consecutive sensor signals into one input. Each input is labeled from 1 to 9 that are pressed by fingers. Therefore, our decoding layer is now transformed to generate 9-dimensional vector representing likelihoods of each 9 classes.

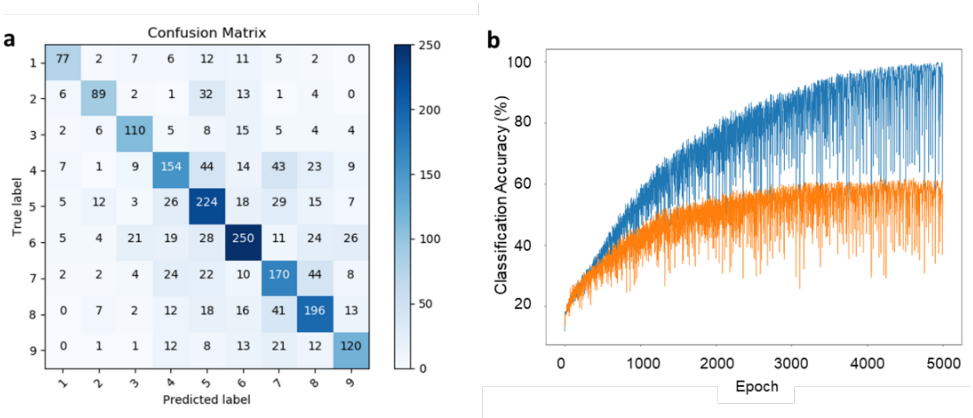

Figure 55. Keypad learning a. Confusion matrix of decoding the keypad typing. b. Classification accuracy of keypad input prediction.

6.6 Predicting the gait motions

To verify the generalizability of our sensor, we also checked whether our model can generate the gait motions of a user using data from a sensor attached to the left side of their pelvis. By recording a 1920 x 1080 resolution video of the user's gait motion while gathering sensor signals, we collected 3145 frames of video data and 5158 points of sensor data.

Each frame was manually labeled with the pixel coordinates of the pelvis, left knee and left ankle, and then synchronized with the sensor values obtained during the frame (Figure 57). The labelled position of the pelvis was fixed for all frames to clearly show gait motion between frames. For sensor values collected between two consecutive video frames, the coordinates of the left knee and ankle were estimated through linear interpolation of their coordinates in the two frames. Just as we preprocessed the data for hand motion generation, we grouped 16 consecutive sensor signals as one input so that our model can utilize the sequential patterns of the sensor signals, with each input labelled with the corresponding gait motion of the last signal within the input.

To generate positions of the ankle and the knee, we modified the last layer of our decoding network to generate a 4-dimensional output vector instead. With 3 dense layers and dropout combined, the decoding network is transformed so that it maps a latent vector generated by the encoding network to two points within the image space of the video. Thus, the first two values of the output vector represent the x and y coordinates of the left knee, while the last two values represent the coordinates of the left ankle. The loss function for our model training (Figure 58) is the mean squared errors between the labeled points and the predicted points. 80% of the sensor frames are used as the training set and the remaining 20% of the sensor frames are used as the testing set. The results of predicting gait motions form the test sets are demonstrated in Figure 57b-c.

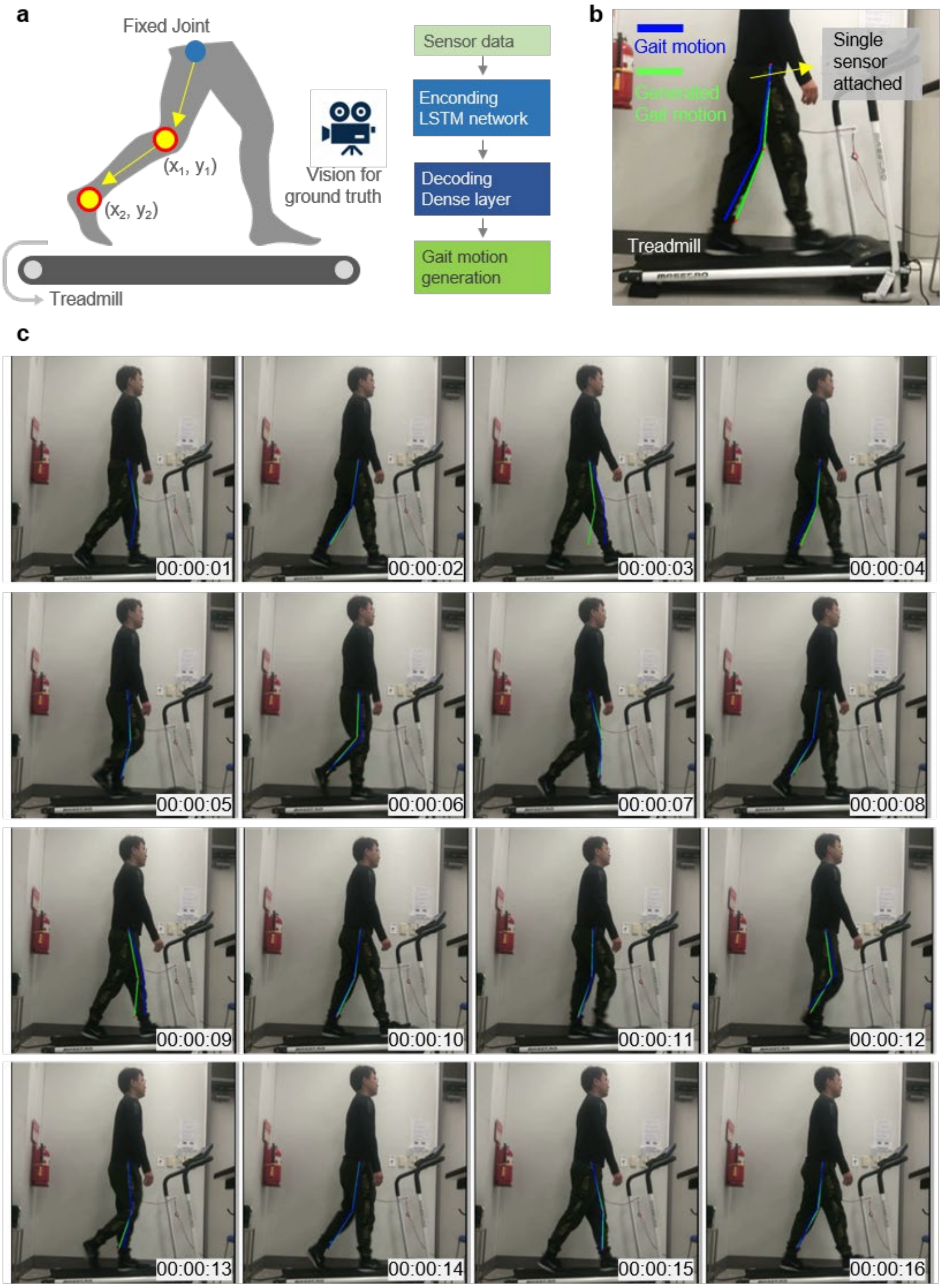

Figure 56. Predicting gait motions by a single sensor attached on pelvis a. Experimental settings of receiving gait signals. b-c. Successfully decoded gait motions.

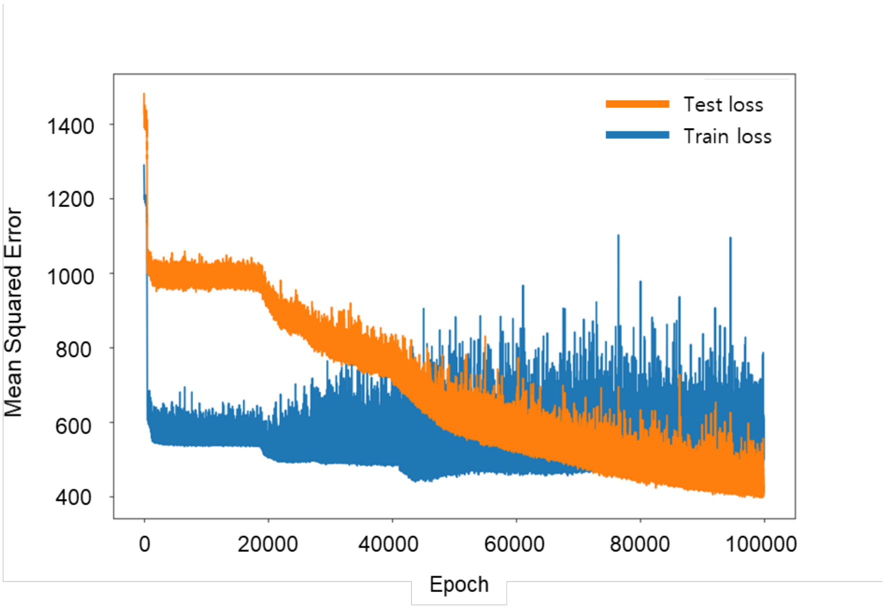

Figure 57. Mean Squared Error for gait motion prediction model.

Chapter VII

Conclusion

- Wearable and transparent 3D touch by laser induced Marangoni flow

We have created a new type of transparent 3D touch, for the first time (to our knowledge), which operates in a single device. The integrated sensor was fabricated through mask-less laser processing of Ag nanoparticles and spray coating of Ag nanowires. The conditions for the various multi-scale structures generated by laser thermal gradient were evaluated and characterized by a dimensionless surface shape number, S. The mechanism of the sensor was precisely investigated by contact mechanics and conformal mapping of the current distribution and a concrete correlation between the surface morphology and the sensor performance was found. The analytical model relating them laid the foundation for determining the design and patterning parameters of the sensor for various applications. With the assistance of the newly suggested 6-wired system, the sensor could assign 3D sensing capability to various surfaces while remaining nearly imperceptible to the user. 3D touch also demonstrated perfect operation in a wearable and wireless environment. This system can have a great impact in the implementation of future wearable devices and brings a powerful new dimension to human-machine interactions.

- A deep learned skin sensor decoding complex human motion

Inspired by the understanding of detection techniques for measuring converging signals, we present a technique for measuring dynamic motions by a deep-learned soft sensor attached on the surface of the skin, that is, superior to conventional approaches. Apart from the traditional wafer-based fabrication, the proposed laser fabrication provides a powerful solution for viable sensor utilization. The relationship between the sensor performance and the controlling parameters was investigated to ensure precise manipulation. A deep neural network is synchronized with the measuring equipment and the sensor, demonstrating a perfect operation in decoding finger motions. The concept of our system is expandable to other body parts, and offers great potential for detecting other stimuli and physiological signals. For device expansion on other body parts, a concrete ergonomic analysis will be needed to select an optimum location to measure epicentral motions. Methods of selecting required number of sensors and technique of integrating with wireless platform is necessary for practical use.

Bibliography

1. Luo, S. et al. Tunable-sensitivity flexible pressure sensor based on graphene transparent electrode. Solid State Electron. 145, 29–33 (2018).

2. Jiang, X. Z., Sun, Y. J., Fan, Z. & Zhang, T. Y. Integrated flexible, waterproof, transparent, and self-powered tactile sensing panel. ACS Nano 10, 7696–7704 (2016).

3. Wang, L. et al. PDMS/MWCNT-based tactile sensor array with coplanar electrodes for crosstalk suppression. Microsyst. Nanosyst. 2, 16065 (2016)

4. Lee, D. et al. High-performance transparent pressure sensor based on seaurchin shaped metal nanoparticles and polyurethane microdome arrays for real-time monitoring. Nanoscale 10, 18812–18820 (2018).

5. Park, J. et al. Giant tunneling piezoresistance of composite elastomers with interlocked microdome arrays for ultrasensitive and multimodal electronic skins. ACS nano 8, 4689–4697 (2014).

6. Park, J., Kim, M., Lee, Y., Lee, H. S. & Ko, H. Fingertip skin–inspired microstructured ferroelectric skins discriminate static/dynamic pressure and temperature stimuli. Sci. Adv. 1, e1500661 (2015).

7. Bae, G. Y. et al. Linearly and highly pressure-sensitive electronic skin based on a bioinspired hierarchical structural array. Adv. Mater. 28, 5300–5306 (2016).

8. Pang, Y. et al. Epidermis microstructure inspired graphene pressure sensor

with random distributed spinosum for high sensitivity and large linearity. ACS Nano 12, 2346–2354 (2018).

9. Kang, D. et al. Ultrasensitive mechanical crack-based sensor inspired by the spider sensory system. Nature 516, 222–226 (2014).

10. Proske, U. et al. The proprioceptive senses: their roles in signaling body shape, body position and movement, and muscle force. Physiol. Rev. 92, 1651–1697 (2012).

11. Totaro, M. et al. Soft smart garments for lower limb joint position analysis. Sensors 17, 2314 (2017).

12. Clites, T. R. et al. Proprioception from a neurally controlled lower extremity prosthesis. Sci. Transl. Med. 10, eaap8373 (2018).

13. Hargrove, L. J. et al. Robotic leg control with EMG decoding in an amputee with nerve transfers. N. Engl. J. Med. 369, 1237–1242 (2013).

14. Tibold, R. et al. Prediction of muscle activity during loaded movements of the upper limb. J. Neuroeng. Rehabil. 12, 6 (2015).

15. Su, M. et al. Nanoparticle based curve arrays for multirecognition flexible electronics. Adv. Mater. 28, 1369–1374 (2016).

16. ElKoura, G. et.al. Handrix: Animating thehuman hand. In Proc. of the 2003

17. ACM SIGGRAPH/Eurographics symposium on Computer animation. 110–119 (Eurographics Association, 2003)

18. Park, B. et al. Dramatically enhanced mechanosensitivity and signal-to-noise ratio of nanoscale crack-based sensors: effect of crack depth. Adv. Mater. 28, 8130–8137 (2016).

19. Han, Z. et al. High-performance flexible strain sensor with bio-inspired crack arrays. Nanoscale 10, 15178–15186 (2018).

20. Lee, E. et al. Effect of metal thickness on the sensitivity of crack-based

sensors. Sensors 18 (2018).

21. Kim, T. et al. Polyimide encapsulation of spider-inspired crack-based sensors for durability improvement. Appl. Sci. 8, 367 (2018).

22. Choi, Y. W. et al. Ultra-sensitive pressure sensor based on guided straight mechanical cracks. Sci. Rep. 7, 40116 (2017).

Abstract

Augmented skin electronics for human-machine interaction based on laser nano structuring and machine intelligence

성 명(Kyun Kyu Kim)

학과 및 전공(Aerospace and Mechanical Engineering)

The Graduate School

Seoul National University

복잡한 시스템의 상태 모니터링에는 많은 수의 센서가 필요하다. 특히 소프트 전자소자에 대한 연구는 체온, 전기 생리 학적 신호, 기계적 긴장과 같은 다양한 자극을 매핑하는 것을 목표로 한다. 그러나 기존의 접근 방식은 대상 영역의 전체 표면을 뒤 덮는 수 많은 센서 네트워크가 필요했다. 본 논문은 하나의 센서만을 활용하여 3 차원 터치 정보와 사람의 움직임을 측정할 수 있는 새로운 전자 스킨에 대해 소개한다. 나노 파티클의 레이저 유도 멀티 스케일 구조를 통해 목표 감도와 성능을 달성할 수 있으며, 딥 뉴럴 네트워크를 활용하여 인체의 움직임을 예측하였다. 이 기술은 건강 모니터링, 동작 추적 및 소프트 로봇 공학의 전환점을 제공 할 것으로 예상된다.

Keywords : 피부형 센서, 레이저 나노 구조, 기계 지능

Student Number : 2016-34392

Acknowledgements

The course of my study has been truly shaped who I am both personally and professionally. Experiences at Seoul National University have always been an exhilarating time of study, and I benefited tremendously from interacting with a lot of other people. I am very grateful to all the people I have crossed with.

I am extremely fortunate to met my advisor, Professor Seung Hwan Ko for his endless support over the last seven years. He always gave me various ideas and persistent advice on my projects. Conversation with Professor Ko has always been exciting, and I learned his enthusiasm and perseverance as a researcher.

I am thankful to my high school mentor, Keun June Lee. It was when I first discovered the joys of research, and these experiences played an important role in my decision to join the graduate program.

I am fortunate to have worked with Professor Chang Soo Han at Korea University. He introduced and guided me to the field of wearable electronics, kindly hosting me at his lab with a range of opportunities. The early experience of publishing a scientific journal with Professor Han has profoundly supported me throughout the course of my studies.

My interest in the human-machine interface has been accelerated with a wonderful experience at the Soft Robotics Research Center. I am especially thankful to Professor Kyu-Jin Cho for allowing me to be involved in various projects. He played an important role in my research on the integration of artificial intelligence and wearable electronics.

Lastly, I deeply appreciate for the unstinting support and love from my family. They sacrificed a lot of things for this dissertation and my career. My dad, Dr. Kim, has always been as my second advisor, providing me with constructive advice and encouragement.